5-2013

Hybrid Photothermal Technique for Microscale Thermal Conductivity Measurement

Zilong Hua

Recommended Citation

Hua, Zilong, "Hybrid Photothermal Technique for Microscale Thermal Conductivity Measurement" (2013). *All Graduate Theses and Dissertations*. 1491.
https://digitalcommons.usu.edu/etd/1491

HYBRID PHOTOTHERMAL TECHNIQUE FOR MICROSCALE THERMAL CONDUCTIVITY MEASUREMENT

by

Zilong Hua

A dissertation submitted in partial fulfillment
of the requirements for the degree

of

DOCTOR OF PHILOSOPHY

in

Mechanical Engineering

Approved:

Dr. Heng Ban Major Professor	Dr. Byard Wood Committee Member
Dr. Leijun Li Committee Member	Dr. Steven Folkman Committee Member
Dr. David Hurley Committee Member	Dr. Mark R. McLellan Vice President for Research and Dean of the School of Graduate Studies

UTAH STATE UNIVERSITY
Logan, Utah

2013

ABSTRACT

Hybrid Photothermal Technique for Microscale Thermal Conductivity Measurement

by

Zilong Hua, Doctor of Philosophy

Utah State University, 2013

Major Professor: Dr. Heng Ban
Department: Mechanical and Aerospace Engineering

Most existing thermal conductivity measurement techniques of nuclear fuel only measure the overall effective thermal conductivity of the fuel, cladding, and gap, with low spatial-resolution. However, damage to nuclear fuel microstructure caused by neutron-irradiation can result in sharp, local changes of thermal conductivity. Additionally, extremely large temperature-gradients (~1600 K/cm) from the fuel centerline to the coolant result in similar gradients of thermal conductivity. Therefore, in pursuit of greater understanding of nuclear fuel performance, the objective of this study was to develop a non-contact thermal conductivity measurement technique to provide micron-sized spatial-resolution capability. Based on photothermal techniques and using both frequency and spatial-domain photothermal reflectance methods, an experimental measurement system was designed, built, and tested for measuring the thermal conductivity of a thin-film coated material with micron resolution. This hybrid method involves separate measurement of thermal diffusivity, D, and thermal effusivity, e, from which, thermal conductivity, $k = (e^2/D)^{1/2}$ is calculated. A detailed parametric analysis using analytical solutions and a numerical model has been performed to guide the experiment and optimize measurement conditions. The measurement system was validated using two calibration samples having thermal conductivities at both the upper and lower limit of the common range of nuclear fuels (~1 – 10 $\mathrm{W\cdot m^{-1}\cdot K^{-1}}$). Sources of experimental errors are discussed qualitatively and the uncertainty of the measurement system for the thermal conductivity range of interest is quantified. The measured error is found to be about 10%, and up to close to 20% for the worst case (upper limit of k range).

An extended application of the modulated laser excitation technique is explored to measure mechanical properties of solid materials. This technique involves obtaining the natural frequencies of different vibrational modes of a cantilever beam sample allowing for the extraction of the elasticity constants of the material. From Neumann's principle, the number of independent elasticity constants is dependent on the symmetry of the material structure. Specifically, symmetries of crystalline materials and composite materials are analyzed. Experimental results of two validation samples with cubic crystal system agreed well with the published values with experimental errors of ~10%.

(118 pages)

PUBLIC ABSTRACT

Hybrid Photothermal Technique for Microscale Thermal Conductivity Measurement

Zilong Hua

In nuclear reactors, the thermal energy generated from the nuclear reactions needs to be transferred all the way through the core of the fuels to the surrounding steam to be utilized. Therefore, thermal conductivity is considered an important thermophysical property of the fuel which needs to be measured. The nuclear fuel microstructure is known to be damaged by neutron-irradiation, which can result in sharp, local changes of thermal conductivity. However, most existing thermal conductivity measurement techniques of nuclear fuel are not able to make high spatial-resolution measurements. The objective of this study was to develop a non-contact thermal conductivity measurement technique to provide micron-sized spatial-resolution capability.

In this study, two lasers are involved for the non-contact feature: one for heating and the other one for detection. A detailed parametric study is performed to optimize measurement conditions analytically and numerically. The numerical work was performed using a finite element model developed in COMSOL Multiphysics. The measurement system was validated using two calibration samples. Sources of experimental errors are discussed qualitatively and quantitatively.

An extended application of the laser-involved technique is explored to measure mechanical properties of solid materials. By measuring the natural frequencies of a cantilever beam, the elasticity constants of the material can be obtained.

ACKNOWLEDGMENTS

First, I would like to express my gratitude to my advisor, Dr. Heng Ban, for his never-ending motivation and inspiration throughout these five years. His words and working attitude have totally changed my life. I respect him no less than my father. I am equally grateful for the help and encouragement that I received from my other advisor, Dr. David Hurley from Idaho National Laboratory. I spent 20 months in his laboratory and his attitude of scientific research has become my motto in my academic career. I would also like to thank my other committee members, Dr. Leijun Li, Dr. Steven Folkman, and Dr. Byard Wood, for their guidance during my graduate studies. Particularly, I would like to thank Dr. Steven Folkman for his kind help in and out of the class in the first semester of my PhD studies when I worked as his teaching assistant.

Also, I would like to thank all my lab mates and staff at Utah State University and Idaho National Laboratory, for all their valuable discussion and selfless helps. Special thanks go to Robert Schley, Colby Jenson, Austin Fleming, Charlie Folsom, Jingwen Mo, and Zhuorui Song. We spent good times together in the past years. They are not only my workmates but also my greatest friends. The same thanks should be sent to Bonnie Ogden, Chris Spall, and Karen Zobell for their great help. I also owe my gratitude to many friends who encouraged me to finish this course. Haiyang Chao, Qi Wang, and Yanzhe Yang gave me lots of useful advice; Xiang Li, Yuanzhi Zheng, and Li Yang always supported me whenever I needed them; and Deming Yuan inspired my interests in other areas of life. Limitation of space prevents me from listing all the names here but I cherish your friendships heart and soul.

I am also grateful to the funding supporter of this project, the Department of Energy, Idaho National Laboratory.

My deepest appreciation goes to my family members. I have been grateful for the help, support, encouragement, and love from my parents and my grandparents in every second of my life.

Zilong Hua

CONTENTS

Page

CHAPTER

LIST OF TABLES

Table Page

LIST OF FIGURES

ACRONYMS

AOM	acousto-optic modulator
B.C	boundary condition
CCD	charged-couple device
COMSOL	COMSOL Multiphysics software package
DP	deviation parameter
EBSD	electron backscatter diffraction
FDPRT	frequency-domain photothermal reflectance technique
GS	general slope
LRUS	laser-based resonant ultrasonic spectroscopy
ODP	overall deviation parameter
OSP	overall slope parameter
PA	photoacoustic
PD	photothermal displacement
PTR	photothermal radiometry
SDPRT	spatial-domain photothermal reflectance technique
SP	symmetry parameter

NOMENCLATURE

C	Stiffness tensor (stiffness constant), [N/m^2]
C_T	Temperature dependent coefficient of thermal conductivity, [N/m^2/K]
D	Thermal diffusivity, [m^2/s]
D_f	Thermal diffusivity of the film, [m^2/s]
D_s	Thermal diffusivity of the substrate, [m^2/s]
D_{eff}	Effective thermal diffusivity, [m^2/s]
E	Young’s modulus, [N/m^2]
G	Shear modulus, [N/m^2]
I	Polar moment of the cross section, [kg·m^2]
L	Length, [m]
L_{th}	Thermal diffusion length, [m]
$L_{th,eff}$	Effective thermal diffusion length, [m]
P	Heating laser power, [W]
Q	Heat flux, [W/m^2]
Q_f	Heat flux into the film, [W/m^2]
Q_s	Heat flux into the substrate, [W/m^2]
R_f	Optical reflectivity of the film
R_s	Optical reflectivity of the substrate
S	Compliance tensor (compliance constant), [m^2/N]
T	Temperature, [K]
T_f	Temperature of the film, [K]

T_s	Temperature of the substrate, [K]
a_1	Major axes of the heating laser beam, [m]
a_2	Minor axes of the heating laser beam, [m]
c	Specific heat capacity, [$J \cdot kg^{-1} \cdot K^{-1}$]
c_f	Specific heat capacity of the film, [$J \cdot kg^{-1} \cdot K^{-1}$]
c_s	Specific heat capacity of the substrate, [$J \cdot kg^{-1} \cdot K^{-1}$]
e	Thermal effusivity, [$J/(m^2 s^{1/2} K)$]
e_f	Thermal effusivity of the film, [$J/(m^2 s^{1/2} K)$]
e_s	Thermal effusivity of the substrate, [$J/(m^2 s^{1/2} K)$]
f	Frequency, [Hz]
h	Film thickness, [m]
k	Thermal conductivity, [$W \cdot m^{-1} \cdot K^{-1}$]
k_f	Thermal conductivity of the film, [$W \cdot m^{-1} \cdot K^{-1}$]
k_s	Thermal conductivity of the substrate, [$W \cdot m^{-1} \cdot K^{-1}$]
q	Thermal wave number, [m^{-1}]
t	Time, [s]
t	(solid mechanics) Thickness, [m]
w	Width, [m]
α	Optical absorption coefficient, [m^{-1}]
α_f	Optical absorption coefficient of the film, [m^{-1}]
α_s	Optical absorption coefficient of the substrate, [m^{-1}]
β	The ratio of the substrate thermal effusivity to the film thermal effusivity
δ	Phase (lag), [deg]
$\delta(x)$	Dirac delta function

ε	Radiation emissivity
ε	(solid mechanics) Strain
ρ	Density, [kg/m^3]
ρ_f	Density of the film, [kg/m^3]
ρ_s	Density of the substrate, [kg/m^3]
σ	Stress, [N/m^2]
τ_f	Characteristic time of the film, [s]
ω	Angular frequency, [Hz]

CHAPTER 1

INTRODUCTION

In this chapter, the essentials of heat conduction are discussed with the important parameters including thermal conductivity, diffusivity, and effusivity, thermal wave, and thermal diffusion length. The significance of this project is stated in the end.

1.1. Heat Transfer and Thermal Transport Properties in Heat Conduction

Heat transfer as a common energy-exchange phenomenon widely exists in solids, liquids, gases, and across the voids of vacuum. The fundamental modes of heat transfers are heat conduction, heat convection, and heat radiation. Heat conduction occurs inside material and across the contact interface between separate bodies. Heat convection occurs between moving fluids and/or surfaces. Heat radiation is the only mode that does not need a medium and occurs between two non-contacting materials. In this work, the mechanism of interest is heat conduction in solids. Three important thermal properties that describe thermal conduction in a continuum are introduced in this chapter: thermal conductivity, thermal diffusivity and thermal effusivity.

1.1.1. Thermal Conductivity

Thermal conductivity is the most important thermal transport property in heat conduction. In current textbooks [1], thermal conductivity is commonly introduced through the one-dimensional (1D) Fourier's law, which states the relation between the heat-flow rate through a homogeneous solid and the temperature gradient along the heat-flow path as:

$$\frac{dQ}{dt} = -kA\frac{dT}{dx} \tag{1.1}$$

where A is the cross section area, and the proportionality ratio k is thermal conductivity. In most literatures, thermal conductivity is denoted as k or λ. It has an SI unit as Watt (W) / meter (m) / Kelvin (K).

Thermal conductivity of different types of materials can vary greatly. Most metals are good thermal conductors with thermal conductivity of ~100 $W \cdot m^{-1} \cdot K^{-1}$, while for glass, wood and concrete the value is comparable to or less than 1 $W \cdot m^{-1} \cdot K^{-1}$. The reason for large variations of thermal conductivity in materials is differences in their microstructures. In metals, free electrons are the primary thermal-energy carriers. For non-metallic crystals that do not have free electrons, the heat conduction mechanism is different. In 1912, Debye stated that the heat conduction mechanism in crystals is the wave motion formed by lattice vibration. To describe the vibrational motion, phonon was introduced by Russian scientist Igor Tamm in 1932. A phonon represents an excited state in the quantum mechanical quantization of the lattice vibrational modes, which can be treated as particles. In modern solid state physics, phonons are considered to be the primary thermal-energy carriers in non-metal crystals [2].

For both metals and non-metallic crystals, thermal conductivity is a function of number density, heat capacity contribution, mean free path, and mean moving velocity of the carriers. The high number-density of free electrons is considered the main reason why most metals are good thermal conductors. In contrast, the low number density and long mean free path of phonons generally lead to low thermal conductivity of non-metals. Still there are several exceptions including diamond, which has the highest recorded thermal conductivity of any bulk solid. Some of these parameters such as mean free path are temperature dependent, leading to the temperature dependence of thermal conductivity. For imperfect materials, thermal conductivity may be dramatically reduced because of the existence of defect, impurity, and boundary scattering in both metals and non-metals.

1.1.2. Thermal Diffusivity

Thermal diffusivity plays an important role in transient heat-conduction procedure. It is defined as thermal conductivity divided by volumetric heat capacity, $\frac{k}{\rho c}$, with the SI unit of m^2/s. The transient heat-conduction equation explicitly contains thermal diffusivity:

$$\nabla^2 T - \frac{1}{D}\frac{\partial T}{\partial t} = -\frac{\dot{Q}}{k} \tag{1.2}$$

Thermal conductivity is a property of a material that describes how well it transports thermal energy. Thermal diffusivity is a material property that describes how fast the temperature of a material responds to an imposed heat flux or a temperature change of surrounding environment. Good thermal conductors generally have high thermal diffusivity as well.

1.1.3. Thermal Effusivity

Thermal effusivity is perhaps the least familiar one of the three thermal parameters being discussed. It is an indicator of a material's ability to exchange thermal energy with its surroundings. In other words, thermal effusivity describes the transient thermal-behavior at the interface of two objects in contact. The temperature of the contact interface between two semi-infinite bodies only depends on the temperatures of the bodies and their effusivities. The definition of thermal effusivity is the square root of the product of a material's thermal conductivity and volumetric heat-capacity, $e = (k\rho c)^{1/2}$, and the SI unit for thermal effusivity is $J/(m^2 s^{1/2} K)$.

An explicit relation of three thermal transport properties can be found as $k = e \times D^{1/2}$. Because thermal conductivity is difficult to extract directly from experimental measurements, the approach used in this work is to measure thermal diffusivity and thermal effusivity separately, from which thermal conductivity can be calculated.

1.2. Thermal Wave and Thermal Diffusion Length

Two important concepts, thermal wave and thermal diffusion length, are introduced in this section to help understand heat conduction and the approach of this measurement. Thermal wave (or temperature wave) was introduced by Carslaw and Jaeger in the classic work, *Conduction of Heat in Solids* [3]. In the book, the temperature expression derived from the thermal conduction equation with harmonic heat source was proved to be a wave-like function, changing periodically in both space and time. This "thermal wave" also showed other wave propagation features such as reflection, refraction and transmission. Since then, the thermal wave has been widely used to describe temperature oscillations produced by a periodic heat-source.

To describe the range of thermal-waves propagation (always in solid materials) from the heat source, thermal diffusion length is defined as $L_{th} = \sqrt{\frac{D}{\pi f}}$. The dependence of the thermal diffusion length on the frequency (f) of a harmonic heat-source is widely utilized to measure thermal properties of multi-layered samples. The definition of thermal diffusion length in the case of pulsed-transient heat source was given by a more traditional way – the distance at which the temperature amplitude of the heat flux reduces to 1/*e* compared to that at heat source.

1.3. Nuclear Reactions and Nuclear Fuels

Nuclear energy is a promising candidate for near-term replacement of traditional fossil fuels. Nuclear fuel has an energy density thousands-of-times more than fossil fuels with near-zero greenhouse gas emission. Nowadays, nuclear power plants provide about 6% of the world's energy and 13-14% of the world's electricity [4].

Commercial nuclear power reactors generally use sustained nuclear fission to generate heat and electricity. The fissile materials that can sustain fission chain reactions are nuclear fuels. The most common nuclear fuels are ^{235}U (the isotope of uranium with an atomic mass of 235) and ^{239}Pu (the isotope of plutonium with an atomic mass of 239). In nuclear reactors, the fissile materials absorb neutrons and split into the fission products, releasing energy, gamma radiation and free neutrons. A portion of these neutrons may later be absorbed by other fissile atoms and trigger further nuclear chain reactions. By using neutron poisons and neutron moderators, nuclear chain reactions can be controlled or stopped if unsafe conditions are detected in nuclear reactors.

1.4. Motivation

Thermal conductivity of nuclear fuel is intimately related to energy conversion efficiency and reactor safety. Due to the microstructure damage caused by neutron irradiation (Fig. 1.1), thermal conductivity of nuclear fuel is known to depend strongly on the local environment, sometimes with extremely sharp changes within a few millimeters. Therefore, a significant need exists to know the thermal conductivity distribution inside nuclear fuel with high spatial-resolution. However, current in-pile measurement techniques, for example, use thermocouples to measure the temperature gradient in the nuclear fuel and only provide an “effective” thermal conductivity of the fuel, cladding and gap [5]. The laser flash technique, another commonly used technique to measure thermal properties of nuclear fuels, also lacks required spatial-resolution to make local measurements [6].

The main motivation of this project is to develop a measurement technique to fill a technology gap. Based on the photothermal reflectance technique, our approach measures thermal conductivity of solid materials (ultimately, nuclear fuels) with micrometer spatial-resolution requiring only a small surface area (typically less than a square millimeter) for measurement. Thus, sample size can be made very small, which is also helpful for handling irradiated nuclear fuel materials.

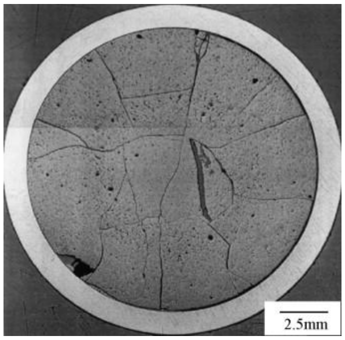

Figure 1.1 A cross-section photo of the post-irradiation nuclear fuel rod (notice the micro cracks) [7].

1.5. Dissertation Overview

This dissertation is divided into four main parts. A literature review, objectives and theoretical models are given in detail in Chapters 2 – 4, respectively. Experimental details are described in Chapter 5 and 6, including the experimental setup, results, and related discussions. In Chapter 7, a numerical model built in finite-element analysis software COMSOL is introduced. The influences on experimental results from some parameters which are impossible to be considered in analytical model are checked in numerical model. Chapter 8 demonstrates an extended project to measure mechanical properties (elasticity constants) of solid materials in the form of a cantilever beam. By examining the change of elasticity constants, it has the potential to detect microstructural changes inside nuclear fuels. In the end, Chapter 9 gives the conclusions and future plans.

CHAPTER 2

LITERATURE REVIEW

In this chapter, photothermal techniques, as the most popular transient technique to measure thermal transport properties with high spatial-resolution, are reviewed. The photothermal reflectance techniques in spatial domain and frequency domain are selected to measure thermal diffusivity and effusivity with the resolution of micrometer range and extract thermal conductivity from thermal diffusivity and effusivity data.

2.1. Traditional Measurements of Thermal Transport Properties

Before photothermal techniques were invented and developed to be mainstream techniques, countless efforts had been made in the development of thermal property measurements. A general classification divides the measurements into two categories. The first is steady-state measurements where a static temperature-gradient is established in a sample from a heat source (e.g., an electrical resistance heater). The temperature difference between two (or more) locations is measured as well as corresponding heat flux. Thermal conductivity can then be derived from Fourier’s law in a straight forward manner. To reach steady state, relatively long time is required to apply the measurements. One annoying problem of steady-state measurements is that the existence of contact resistance from thermometers makes the measurements difficult to carry out for good thermal conductors. Nowadays this technique is still employed in some areas if local thermal conductivity is not required and the sample thermal conductivity is not high.

As opposed to steady-state methods, transient methods measure time-dependent temperature responses to a heat excitation, and obtain properties based on the transient heat conduction equation. A further distinction for transient methods is that the heat source can be a periodic or short-duration transient. Periodic heating was first introduced to measure thermal diffusivity by Angstrom in 1861 [8]. In this classic method, a harmonic heat source is applied to a sample to create periodic temperature variation, and the thermal diffusivity can be derived from either the variation of the amplitude or phase of the induced thermal wave at different locations. Another type of transient methods is to use a pulsed heat source instead of a harmonic heat source. Thermal properties can be derived from the temperature response of the sample after the short excitation. These two types of transient methods are the basis of current photothermal techniques in frequency domain and time domain respectively.

Undoubtedly, the equations of analytical solutions for transient methods are more complicated than the ones for steady-state methods. However, steady-state methods can only measure thermal conductivity with low spatial-resolution for a bulk solid with one surface available for measurement. Given proper boundary conditions and a well-defined heat source, more thermal transport properties can be obtained from non-steady-state methods with good spatial accuracy.

2.2. Photothermal Techniques

With more than 30 years of development, photothermal techniques have been widely accepted as one of the best options to measure thermal transport properties of materials with high spatial-resolution. In a typical photothermal setup, a pump laser is used as a transient heat-source, modulated either in the frequency domain (amplitude-modulated continuous-wave laser), or in the time domain (short-duration pulsed laser). The means of the temperature-change detection caused by the thermal-wave propagation are different in various approaches. Often, another laser (termed the probe laser) is used in one of several different manners including: detecting the thermally-induced deformation of the surface (i.e., photothermal displacement technique), measuring the temperature gradient (refraction index gradient) of the surrounding gas above the heated surface (i.e., photothermal deflection technique), or sensing small temperature-induced changes in optical reflectivity of the heated surface (i.e., photothermal reflectance technique). For some photothermal techniques the probe laser is not necessary, such as the photothermal radiometry technique, in which the radiated heat from surface is collected by an infrared detector.

Laser-based photothermal techniques have several intrinsic advantages: the measurements are non-contact and non-destructive and can be done in a relatively short time; micrometer spatial-resolution is possible with proper laser selection and modulation. A considerable number of studies have been published on measuring thermal conductivity, diffusivity and effusivity of a wide variety of solid materials, liquids and gases. A brief review of the literatures of popular photothermal techniques is presented in the following sections.

2.2.1. Photoacoustic Technique and Laser Flash Technique

The sound waves generated by thermal expansion upon photothermal heating can be detected acoustically, resulting in a separate category of measurements known as the photoacoustic (PA) technique. Periodic thermal expansion and contraction of the sample surface causes the surrounding gas-layer to expand and compress periodically, generating a detectable acoustic-signal. After the PA effect was first discovered by Alexander Graham Bell in 1880, new technologies, such as microphone and lock-in amplifier, have been added in to improve the detection sensitivity. By the early 1970s, development of the laser had made the PA technique widely used to measure thermal properties. The PA technique was first applied to measure thermal diffusivity in 1975 by Rosencwaig and Gersho [9]. By including the optical-thermal energy conversion term in heat diffusion equations, they derived the AC component of the temperature distribution and the gas displacement under periodic laser-excitation as functions of the thermal diffusivities of the gas and sample. Using similar theories, thermal diffusivity and conductivity of some materials have been measured [10, 11].

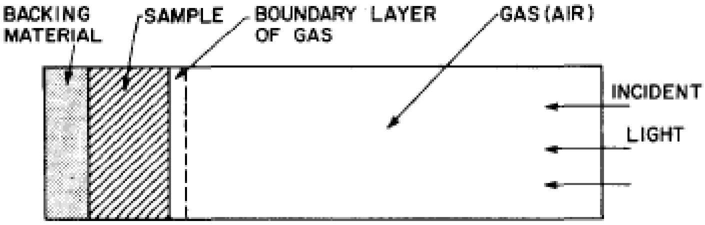

Figure 2.1 Photoacoustic effect: light – acoustic energy conversion [9].

Another famous laser-based technique to measure thermal transport properties is the laser flash technique, introduced by Parker in 1961 [12]. Due to the technology limitations at the time, a flash tube was initially used as the heat source but later lasers have become the standard. The principle of the technique is to detect the diffusion speed of a thermal energy pulse travelling through a sample by pulsed heating on the front surface of a sample and measuring the temperature change of the rear surface. The time-dependent feature of the laser flash technique leads its main application to measure the thermal diffusivity of a large range of solids and liquid materials, including bulk materials, coatings, composites, polymers and glasses [13-15].

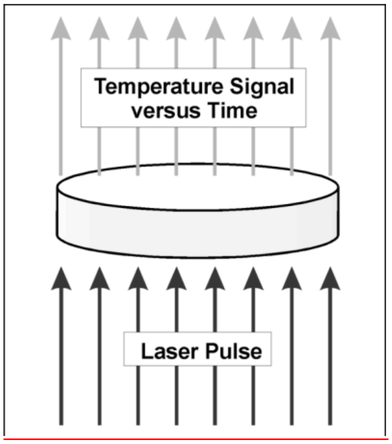

Figure 2.2 Laser flash technique [16].

Although the PA, laser flash and other photothermal techniques are essentially based on the same thermal transport theory, differences exist in data from different techniques. The mechanism of the PA technique is to detect induced acoustic effects to reflect the delay in the temperature response to the period heating. In the laser flash technique only diffusion speed of thermal flux is determined from a combined effect of the amplitude and phase delay of the temperature wave propagation through the sample. In many other photothermal techniques, the amplitude and phase changes due to thermal-wave propagation and scattering can be obtained individually, which can provide a better local thermal properties measurement.

2.2.2. Photothermal Displacement Spectroscopy

Photothermal displacement (PD) spectroscopy was introduced by Olmstead in 1983 [17]. The principle of the PD technique is to use a modulated pump laser beam to generate a regional temperature fluctuation and thermoelastic deformation on sample surface, which is detected by the variation of the reflection angle of an incident probe laser beam. By analyzing the variation of the reflection angle in frequency domain or time domain, the sample optical absorption, thermal expansion coefficient, thermal diffusion length and thermal conductivity can be determined [18-20]. To perform this technique on thermal conductivity measurement needs information of the thermal expansion coefficient and Poisson ratio. These additional parameters bring uncertainty and signal-to-noise ratio issues to the thermal properties determination.

2.2.3. Photothermal Deflection Technique

In 1979 Boccara, Fournier and Badoz proposed the photothermal deflection technique (they named it “photoacoustic spectroscopy” as an evolution from the PA technique) [22]. It detects the refractive index gradient associated with the temperature gradient of the surrounding gas on the heated surface which is also called “mirage effect.” A general setup includes a pump laser to generate thermal wave on a sample surface, a probe laser to detect the refractive index

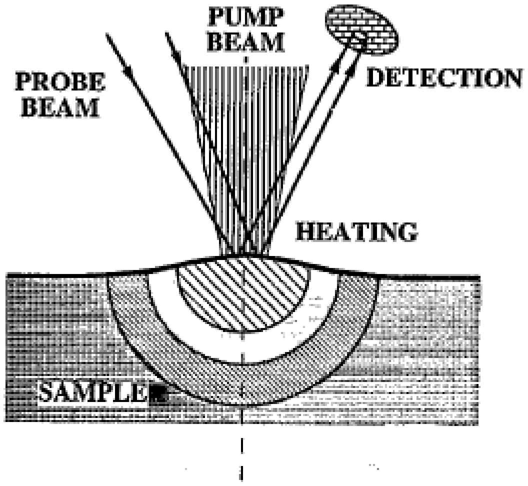

Figure 2.3 Mechanism of the photothermal displacement technique: thermophysical deformation caused by heating [21].

gradient by passing through the heated gas, and a position-sensing detector to monitor the probe beam deflection. By plotting the recorded deflection angle as a function of the wavelength of the heating laser beam Boccara obtained the photothermal spectroscopy ("photoacoustic spectroscopy" in ref. 17 and 18) and the coefficient of optical absorption was derived [20, 23]. A few months later, the relationship of the deflection beam angle/amplitude to the thermal properties of the gas was derived from a similar setup by Murphy and Aamodt [24] and the photothermal deflection technique was formally introduced. Despite the incapability of performing precise local measurements, the photothermal deflection technique has received significant development and has been applied for measuring thermal properties of many materials [25-27].

2.2.4. Photothermal Radiometry

Based on the detection of blackbody thermal radiation, photothermal radiometry (PTR) is another well-established photothermal technique. In a typical PTR approach, the transient thermal-flux emitted from the heated sample surface is collected by a cooled photoconductivedetector. This technique was first introduced by Nordal and Kanstad in 1979 as an alternative to the traditional spectroscopic analysis of solid and semisolid materials [28]. Santos and Miranda worked out a quantitative derivation of the PTR signal in frequency domain and time domain involving optical absorption in 1981. The results showed the capability of the PTR technique to measure thermal diffusivity and the coefficient of optical absorption of solids [29]. To date, several PTR theoretical models have been developed and applied to measure thermal properties of various solid materials [30-33].

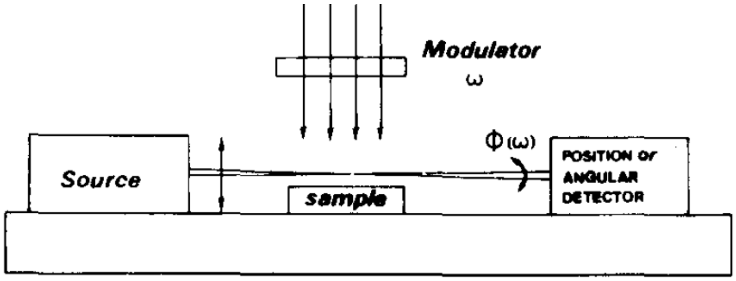

Figure 2.4 A typical setup of the photothermal deflection technique [22].

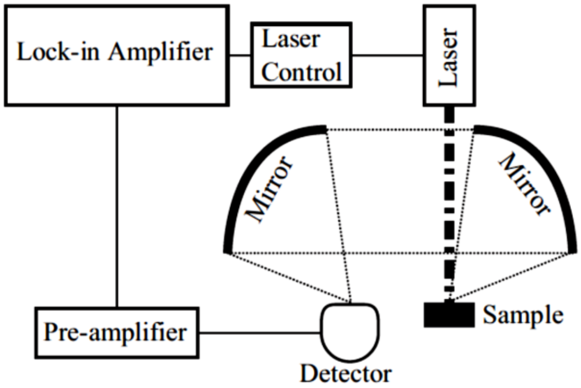

Figure 2.5 A typical setup of photothermal radiometry [33].

2.2.5. Photothermal Reflectance Technique

The change of the optical reflectivity of a solid material can be considered as a linear function of the temperature change (in a moderate temperature range) [34]. This phenomenon was first utilized on the photothermal reflectance technique by Rosencwaig in 1985 [35]. The rate of optical reflectivity change to temperature change is defined as the temperature coefficient of optical reflectivity. A typical photothermal reflectance system includes a pump laser as a modulated heat source in frequency domain [36-38], time domain [39] or spatial domain [40, 41] and a continuous-wave probe laser (or a split branch of the pump laser before modulation) to detect the optical reflectivity change as an indicator of the temperature change. Depending on different boundary conditions, thermal conductivity, diffusivity and effusivity can be measured. Performing this technique requires a sample that has a large temperature coefficient of optical reflectivity, high absorptivity at the pump laser wavelength and high reflectivity at the probe laser wavelength. These requirements can be satisfied by coating a particular metal film which absorbs photons at specified wavelengths on the sample. The sample is usually polished to enhance the overall reflectance.

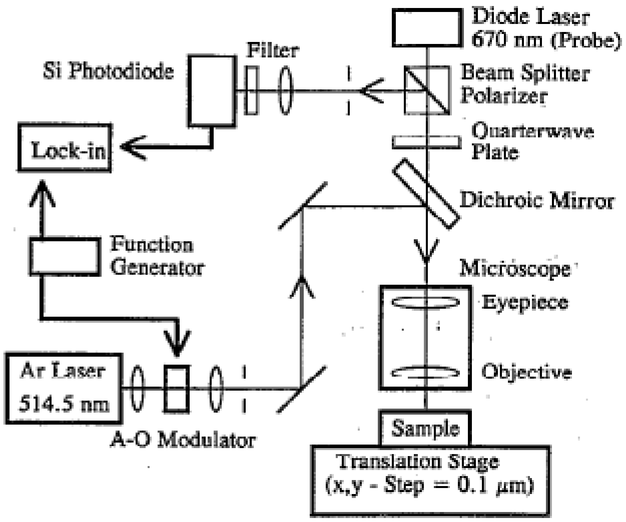

Figure 2.6 A typical setup of the photothermal reflectance technique [42].

2.3. Conclusion of Literature Review

Based on the review of the literature, the photothermal reflectance technique was found to be the most promising option to make thermal conductivity measurements with micrometer resolution. The laser flash method lacks local measurement ability; signal intensity of the photoacoustic, photothermal deflection, and photothermal displacement techniques depend heavily on the measurement setup, thus signal-to-noise ratio is very difficult to guarantee; PTR technique requires sample black-body radiation and has a resolution limitation.

Based on the photothermal reflectance technique in the spatial domain (SDPRT) and frequency domain (FDPRT), numerous measurements have been reported to obtain thermal properties with high spatial-resolution successfully. SDPRT, first reported by Fanton [43], is essentially a recall of Angstrom's method to detect the phase-lag on a sample surface caused by the separation of the pump and probe lasers. For the samples composed of a single material, thermal diffusivity can be derived from the slope of the phase-lag (Fig. 2.7) in a straightforward manner. The details are discussed in Chapter 4.

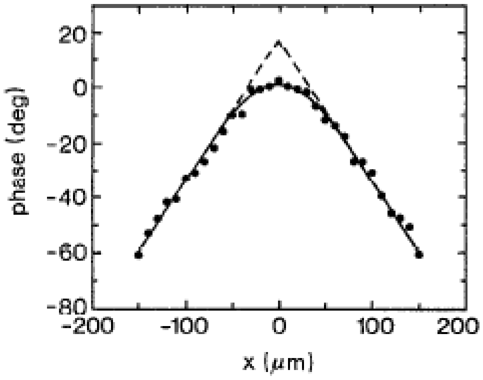

Figure 2.7 An example of SDPRT experimental data: x-axis represents the separation distance between the heating laser and the probe laser, and y-axis represents the phase-lag caused by the separation [37].

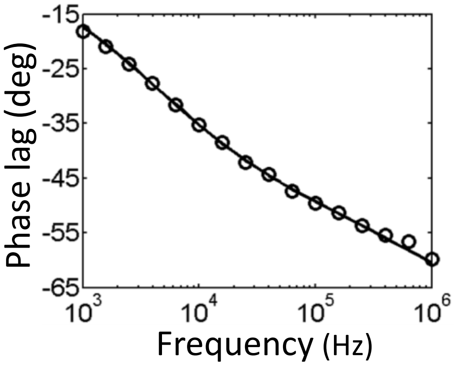

Figure 2.8 An example of FDPRT experimental data [44].

Different from SDPRT, in FDPRT, both lasers are kept concentric while varying heating frequency and recording the phase-lag of the corresponding temperature. FDPRT is one of the most popular methods to obtain thermal properties of film-substrate structure samples because the detection depth (thermal diffusion length) decays with thermal wave modulation frequency. Applying FDPRT with 1D heating, thermal effusivity has been reported successfully measured from the phase-lag vs. frequency plot [45].

A combination of SDPRT and FDPRT is concluded to be the best option for thermal conductivity measurement in this project. By measuring thermal diffusivity and effusivity of the sample (in this case, the substrate in a layered structure), thermal conductivity can be deduced from the explicit relation $k = e \times D^{1/2}$. Depending on the thermal diffusion length and laser spot sizes, spatial resolution of this hybrid system can reach the micrometer level. The utilization of frequency-dependent thermal diffusion length in FDPRT also makes it a good option for measuring interface resistance between layers or detecting subsurface defects[21, 42, 46, 47]. Recently, by using fiber lasers instead of diode lasers, Yarai has reported to compact a FDPRT system into a laptop-size case, which makes the in-situ measurements possible [48].

CHAPTER 3

OBJECTIVES

The overall goal of this work is to develop a hybrid photothermal reflectance system to measure thermal diffusivity and effusivity in spatial and frequency domains, respectively, and thus determine thermal conductivity of solid samples with high spatial-resolution. Ultimately, this approach will be performed on nuclear fuel to obtain the thermal conductivity distribution with micrometer resolution. The specific objectives include:

- Based on the photothermal reflectance technique in frequency domain, establish a theoretical model including interface resistance and absorption coefficient to measure thermal effusivity;
- Design and build a hybrid photothermal reflectance setup to measure thermal effusivity and diffusivity, and optimize this system by performing a detailed parametric analysis of the parameters of interest from the analytical and numerical models (COMSOL Multiphysics);
- Validate the method by performing the measurement on samples having thermal conductivity at both the upper and lower limit of the common range of nuclear fuels;
- Determine experimental uncertainty.

CHAPTER 4

THEORY DEVELOPMENT

In order to obtain thermal conductivity, k, the 1D frequency-domain and spatial-domain photothermal reflectance techniques are used to measure thermal effusivity, e, and diffusivity, D, separately. In this chapter, theoretical details of the measurements are discussed. The existing 1D model to measure e does not consider thermal contact resistance (or “Kaptiza resistance”), R_{th}, and optical absorption coefficient, α, which is shown to be insufficient by our improved model. A 3D model with anisotropic thermal conductivity of both layers is built and mathematically solved to give the analytical solution, from which the sensitivity analysis is carried out.

4.1. Frequency-Domain Photothermal Reflectance Technique (FDPRT)

The basic idea of the frequency-domain photothermal reflectance technique is to periodically modulate the intensity of the heating laser and record the corresponding in-phase temperature change of the heated area (from a probe laser beam reflected off the sample surface). The phase-lag profile, which is a function of the modulation frequency, carries the information that indicates thermal properties of the sample. Depending on the heating condition, i.e., the relationship of the heating area to the thermal diffusion length, L_{th}, theoretical models can be formulated in 1D and 3D coordinates. Theoretically, using a 3D model provides greater flexibility in terms of the number of parameters that can be explored. In practice, however, the added complexity of 3D models always causes sensitivity issues to the parameters of interest, thus lowering the confidence of experimental results. Additionally, in most measurements based on 3D models, an inverse multi-parameter fitting process is required to extract the parameters that exist implicitly in the analytical solution. This process is always tedious and the uniqueness of the solution is hardly guaranteed. On the other hand, e_s of a two-layer sample can be measured from a less complicated fixed-frequency experiment based on a 1D model. As a consequence, the frequency-domain measurement based on a 1D model is selected for e_s extraction. The derivation is given in the following sections.

4.1.1. *Existing 1D Model*

As stated previously, e is introduced from the interface between the film and substrate layers. Without a metal film coated on a thermally thick sample, the phase of the 1D model is independent of any thermal property and results in a constant value of -π/4 regardless of the modulation frequency. In the layered model, e_s is a function of the film properties and modulation frequency. If the thickness and the thermal properties of the film are known, e_s is the only free variable in the phase expression and can be extracted from a fixed-frequency measurement. The first successful measurement was reported by Yagi et al. [38]. The assumptions of the 1D model used in that manuscript include:

1) 1D sinusoidal heating condition is supplied;
2) the substrate layer is semi-infinite in both radius and depth directions;
3) the film layer is semi-infinite in radius direction;
4) contact thermal resistance, R_{th}, at the interface is negligible.

The governing equations in this 1D model can be stated as

$$k_f \frac{\partial^2 T_f}{\partial x^2} - \rho_f c_f \frac{\partial T_f}{\partial t} = 0 \qquad 0<x<h \tag{4.1}$$

$$k_s \frac{\partial^2 T_s}{\partial x^2} - \rho_s c_s \frac{\partial T_s}{\partial t} = 0 \qquad x>h \tag{4.2}$$

where subscripts f and s indicate film and substrate separately, and h is the thickness of the film, with the boundary conditions

$$-k_f \frac{\partial T_f}{\partial x}\Big|_{x=0} = Q_0 \sin(\omega t) \qquad \text{B.C 1)}$$

$$T_f|_{x=h} = T_s|_{x=h} \qquad \text{B.C 2)}$$

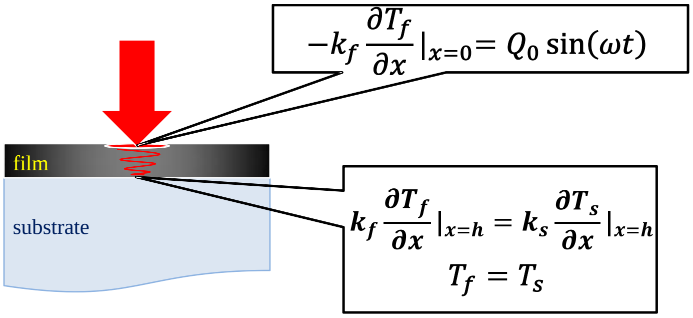

Figure 4.1 The layered model and boundary conditions in the basic 1D model.

$$k_f \frac{\partial T_f}{\partial x}|_{x=h} = k_s \frac{\partial T_s}{\partial x}|_{x=h} \qquad \text{B.C 3)}$$

The layered model and corresponding boundary conditions are plotted in Fig. 4.1. The phase-lag of the temperature response to the heat source is expressed as

$$-\delta = \frac{3}{4}\pi + \tan^{-1}\left(\frac{\cosh^2\sqrt{\frac{\omega\tau_f}{2}}\left(\tanh\sqrt{\frac{\omega\tau_f}{2}}+\beta\right)\left(\tanh\sqrt{\frac{\omega\tau_f}{2}}+\beta^{-1}\right)}{\cos^2\sqrt{\frac{\omega\tau_f}{2}}\left(\beta-\beta^{-1}\right)\tan\sqrt{\frac{\omega\tau_f}{2}}}\right) \qquad (4.3)$$

where $\beta = e_s/e_f$ and $\tau_f = h^2/D_f$.

In all assumptions of this 1D model, 1D heating is the most important one. Ideally, the 1D heating condition can only be satisfied by using an infinite large heat source with uniform heat flux to heat the whole sample surface. In laser-based measurements, a rule of thumb to satisfy 1D heating is to make heating laser spot size 10 times larger than the thermal diffusion length, L_{th}. It requires a large beam size and high modulation frequency of the heating laser. In most 1D frequency-domain measurements, the heating laser is modulated to megahertz or higher, thus L_{th} in the film layer is comparable to 1 μm. In this case, a size of 10 μm is the bottom-line of the heating laser spot in order to satisfy the 1D heating assumption.

The other assumptions also need to be verified. For a sample with dimensions ~ 1 mm with a coating spanning the entire measured surface, assumptions 2) and 3) are valid. However, R_{th}, which is ignored in assumption 4), is always found at the interface between the film and substrate layers. The existence of R_{th} significantly affects thermal wave propagation and e_s measurement result. Sensitivity analysis in Section 4.3 also shows that the sensitivity curves on e_s and R_{th} have the same peak position. In an extreme case of both layers being good thermal conductors (e.g., metal), the existence of R_{th} can dominate the thermal wave propagation, thus make it impossible to extract thermal properties.

As a consequence, it is important to add R_{th} into the 1D model and quantitatively discuss its influence to the experiment. An improved 1D model is required.

4.1.2. *Improved 1D Model*

In this section, the existing 1D model is revised to include the influence of R_{th} in the measurement of e_s. Additionally, an implicit assumption in the basic model is examined and modified to make the improved model more representative of reality: the heat flux from the pump laser is no longer fully absorbed on the surface of the coating film but within a small volume (depth in the 1D model) of the film layer. It introduces a new parameter, optical absorption coefficient, α, to the improved model.

To prove the use of the implicit surface heating condition in the basic 1D model, governing equation of heat conduction in film is redefined as

$$k_f \frac{\partial^2 T_f}{\partial x^2} - \rho_f c_f \frac{\partial T_f}{\partial t} = Q_0 \sin(\omega t) \times \delta(\mathrm{x}) \tag{4.1*}$$

The added Dirac delta function $\delta(x)$ represents the surface heating condition and diminishes by applying the Fourier transform so that it does not influence the phase-lag expression. This confirms the application of the implicit surface heating assumption in the basic model. It is worth noting that the unit of Q_0 needs to be modified with respect to the unit of the Dirac delta function.

Comparing to R_{th}, the influence of α to the experimental result is expected minor because most laser energy does not penetrate deep into the metal film. Based on the wavelength of the pump laser and the coating material used in this project, the literature value of the optical absorption depth (α^{-1}) is about 10 – 20 nm, which is one or two digits smaller than L_{th} (in our case at the measurement frequency of 1 MHz, L_{th} is about 1 μm). Nevertheless, we still decide to add this parameter to the improved 1D model for a couple of reasons: a different coating material or laser with different wavelength may change the optical absorption depth; a higher measurement frequency will shorten L_{th} and decrease the contrast between L_{th} and the optical absorption depth. If the heating laser is modulated in the frequency range of gigahertz, the volume absorption effect will become significant.

The governing equation to describe the heat conduction in the film layer needs to be rewritten to include α:

$$k_f \frac{\partial^2 T_f}{\partial x^2} - \rho_f c_f \frac{\partial T_f}{\partial t} = Q_0 \sin(\omega t) \exp(-\alpha x) \qquad (4.1)'$$

The boundary conditions correspondingly become

$$-k_f \frac{\partial T_f}{\partial x}|_{x=0} = 0 \qquad \text{B.C 1)'}$$

$$k_f \frac{\partial T_f}{\partial x}|_{x=h} = k_s \frac{\partial T_s}{\partial x}|_{x=h} \qquad \text{B.C 2)'}$$

$$-R_{th} k_s \frac{\partial T}{\partial x}|_{x=h} = T_f - T_s \qquad \text{B.C 3)'}$$

The added R_{th} is in the modified boundary conditions 3)’.

The derivation is a bit lengthy and only the result is given here. The expression of the surface temperature response is $T_0 = \frac{H_0(H_1 - H_2)}{H_3 + H_4} + P$, and

$$H_0 = 2 \frac{Q_0}{k_f} \frac{1}{\alpha^2 - \sigma^2}$$

$$H_1 = \frac{\alpha}{\sigma} \exp(\sigma h) + \exp(-\alpha h)$$

$$H_2 = \frac{\alpha}{\lambda}\frac{k_f}{k_s}(Rthk_s\lambda + 1)[\exp(-\alpha h) - \exp(\sigma h)]$$

$$H_3 = \exp(\sigma h) + \exp(-\sigma h)$$

$$H_4 = \frac{\sigma}{\lambda}\frac{k_f}{k_s}(Rthk_s\lambda + 1)[\exp(\sigma h) - \exp(-\sigma h)]$$

$$P = -\frac{Q_0}{k_f}\frac{1}{\alpha^2-\sigma^2}(1 + \frac{\alpha}{\sigma}) \tag{4.4}$$

where $\sigma = \sqrt{\frac{i\omega}{D_f}}$ and $\lambda = \sqrt{\frac{i\omega}{D_s}}$. Phase-lag δ is obtained from

$$\delta = \tan^{-1}(\frac{Imag(T_0)}{Real(T_0)}) \tag{4.5}$$

The details of derivation can be found in Appendix A.

At first glance, it appears that e_s cannot be extracted because of the existence of the substrate thermal conductivity (k_s) and diffusivity (D_s, contained in λ) terms in H_2 and H_4. However, a little more investigation reveals that all terms containing k_s and D_s are only in the form of the combination $k_s\lambda$ and a simple relation exists to convert them to e_s:

$$k_s\lambda = k_s\sqrt{\frac{i\omega}{D_s}} = \sqrt{i\omega}e_s \tag{4.6}$$

If the coating layer material and heating laser wavelength are both determined, R_{th} and α can be obtained from literatures. Take our experiment as an example. In order to guarantee a good signal-to-noise ratio (which requires a high temperature coefficient of optical reflectivity), the sample needs a Titanium coating and the heating laser needs a wavelength of 532 nm. Based on these selections, the literature value of R_{th} (between Titanium and other material) is approximately 5×10^{-9} Km^2/W [49], and α is 6×10^{7}m^{-1} [50]. Therefore, if the film properties are all known, e_s can still be obtained as the only free variable from a fixed-frequency measurement as in the basic model.

The phase-lags solved from the basic and improved 1D model analytical solutions with respect to the modulation frequency are plotted in Fig. 4.2. All parameters used in the simulation are listed in Table 4-1. A deviation of approximately 0.3 degree is found at 1 MHz between the basic and improved models. Depending on the materials, film thickness, α, and R_{th} at the interface, this deviation can go up to a few degrees and lead up to a 10% error of e_s measurement. If a stronger influence of R_{th} is found or an accurate value of R_{th} is needed, it can be added as the second fitting parameter with e_s and an inverse fitting process will be necessary. In that case, a frequency scan in the 1D heating region (e.g., 1 MHz – 5 MHz in this experiment) is required instead of the fixed-frequency measurement, and the uniqueness of the solution needs to be examined as well.

An interesting result is noticed from Fig. 4.2 that the sole influence of α at the measurement frequency is obviously larger than what we predicted. A reasonable explanation is that the optical absorption depth (about 17 nm) is smaller but still comparable to the film thickness (170 nm), thus the temperature distribution of the film in the depth direction is different from the surface heating condition case.

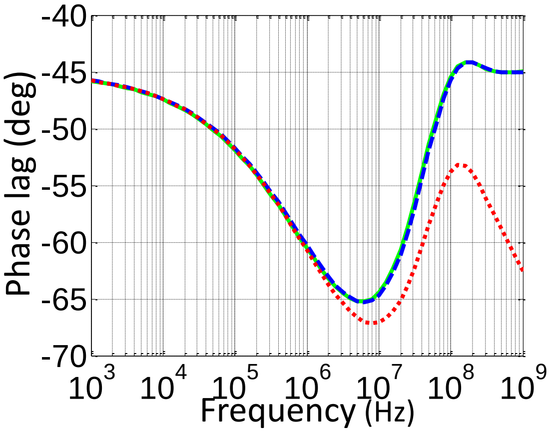

Figure 4.2 Phase lag curves from the basic 1D model (green line), improved 1D model (red dot) and improved 1D model with only Rth considered (blue dash line).

Table 4-1 The parameters used in 1D basic and improved models for simulation.

Parameters	Unit	Basic model	Improved model
k_f	$W \cdot m^{-1} \cdot K^{-1}$	9.6	
ρ_f	kg/m^3	4506	
c_f	$J \cdot K^{-1} \cdot kg^{-1}$	523.5	
k_s	$W \cdot m^{-1} \cdot K^{-1}$	1.4	
ρ_s	kg/m^3	2200	
c_s	$J \cdot K^{-1} \cdot kg^{-1}$	670	
h	nm	170	
R_{th}	Km^2/W	N/A (0)	5×10^{-9}
α	m^{-1}	N/A (∞)	6×10^{7}

4.1.3. 3D model

In order to validate the improved 1D model and carry out sensitivity analysis on the parameters of interest, a more complicated model is built and analyzed in 3D Cartesian coordinate system. The model and coordinate system are plotted in Fig. 4.3. It is worth noting that in the 3D model, the heat source term is described by a Gaussian distribution function.

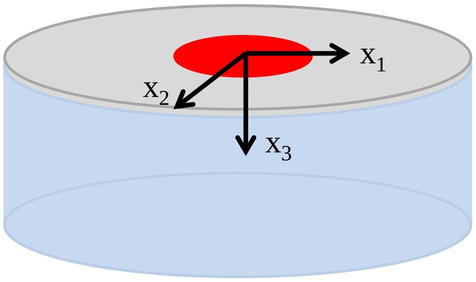

Figure 4.3 The 3D model and coordinate system.

Governing equations in the 3D model are given below with the heat source terms. The boundary conditions are fundamentally the same from the improved 1D model.

$$k_{fij}T_{f,ij} - \rho_f c_f \dot{T}_f = Q_f \tag{4.7}$$

$$k_{sij}T_{s,ij} - \rho_s c_s \dot{T}_s = Q_s \tag{4.8}$$

and the heat source terms are

$$Q_f = \frac{P\alpha_f(1-R_f)}{\pi a_1 a_2}\exp\left(-\frac{x_1^2}{a_1^2} - \frac{x_2^2}{a_2^2} - \alpha_f x_3\right)\left(\frac{1}{2} + \frac{1}{4}(\exp(i\omega t) + \exp(-i\omega t))\right) \tag{4.9}$$

$$Q_s = \frac{P\alpha_s(1-R_f)(1-R_s)\exp(-\alpha_f h)}{\pi a_1 a_2}\exp\left(-\frac{x_1^2}{a_1^2} - \frac{x_2^2}{a_2^2} - \alpha_s(x_3 - h)\right)\left(\frac{1}{2} + \frac{1}{4}(\exp(i\omega t) + \exp(-i\omega t))\right) \tag{4.10}$$

where P is the power of the heating laser, a_1 and a_2 are the major and minor axes of the heating laser beam (a_1=a_2 if the heating laser spot has a circular shape), and R is the reflectivity on the surface of layers. Anisotropic thermal conductivity in both layers is considered in this model with the directions denoted by the subscripts *i* and *j*.

The surface temperature is derived in Fourier space as $\widehat{T_0}(\xi_1, \xi_2)$ with ξ_1 and ξ_2 as the integral variables. It can be derived that $\widehat{T_0}(\xi_1, \xi_2) = A(\xi_1, \xi_2) + B(\xi_1, \xi_2) + E(\xi_1, \xi_2)$, with A and B from boundary conditions:

$$N \cdot \begin{bmatrix} A \\ B \\ C \end{bmatrix} = R$$

and

$$N_{11} = (-ik_{f31}\xi_1 - ik_{f32}\xi_2 - \eta_f k_{f33})$$

$$N_{12} = (-ik_{f31}\xi_1 - ik_{f32}\xi_2 + \eta_f k_{f33})$$

$$N_{13} = 0$$

$$N_{21} = (-ik_{f31}\xi_1 - ik_{f32}\xi_2 - \eta_f k_{f33})\exp(-\eta_f h)$$

$$N_{22} = (-ik_{f31}\xi_1 - ik_{f32}\xi_2 + \eta_f k_{f33})\exp(-\eta_f h)$$

$$N_{23} = (ik_{s31}\xi_1 + ik_{s32}\xi_2 + \eta_s k_{s33})$$

$$N_{31} = R_{th}\left(ik_{f31}\xi_1 + ik_{f32}\xi_2 + \eta_f k_{f33}\right)\exp\left(-\eta_f h\right) - \exp\left(-\eta_f h\right)$$

$$N_{32} = R_{th}\left(ik_{f31}\xi_1 + ik_{f32}\xi_2 - \eta_f k_{f33}\right)\exp\left(\eta_f h\right) - \exp\left(\eta_f h\right)$$

$$N_{33} = 1$$

$$R_1 = E(ik_{f31}\xi_1 + ik_{f32}\xi_2 + \alpha_f k_{f33})$$

$$R_2 = E(ik_{f31}\xi_1 + ik_{f32}\xi_2 + \alpha_f k_{f33})\ \exp\left(-\alpha_f h\right) - F(ik_{s31}\xi_1 + ik_{s32}\xi_2 + \alpha_s k_{s33})$$

$$R_3 = E[1 - R_{th}\left(ik_{f31}\xi_1 + ik_{f32}\xi_2 + \alpha_f k_{f33}\right)]\ \exp\left(-\alpha_f h\right) - F \tag{4.11}$$

where *E* and *F* are obtained from the particular solution as

$$E = \frac{\dfrac{P\alpha_f(1-R_f)}{2\pi}\exp(-\xi_1^2 a_1^2/4 - \xi_2^2 a_2^2/4)}{k_{f33}\alpha_f^2 + 2\alpha_f\left(ik_{f31}\xi_1 + ik_{f23}\xi_2\right) - 2\xi_1\xi_2 k_{f12} - k_{f11}\xi_1^2 - k_{f22}\xi_2^2 - i\omega\rho_f c_f}$$

$$F = \frac{\frac{P\alpha_S(1-R_f)(1-R_S)\exp(-\alpha_f h)}{2\pi}\exp(-\xi_1^2 a_1^2/4 - \xi_2^2 a_2^2/4)}{k_{s33}\alpha_s^2 + 2\alpha_s(ik_{s31}\xi_1 + ik_{s23}\xi_2) - 2\xi_1\xi_2 k_{s12} - k_{s11}\xi_1^2 - k_{s22}\xi_2^2 - i\omega\rho_s c_s} \tag{4.12}$$

and η_f and η_s are parameters defined from the homogenous solutions and can be obtained by applying the homogenous solutions to the diffusion equations:

$$k_{f/s33}\eta_{f/s}^2 + 2i(\xi_1 k_{f/s13} + \xi_2 k_{f/s23}) - 2\xi_1\xi_2 k_{f/s12} - \xi_1^2 k_{f/s11} - \xi_2^2 k_{f/s22} - i\omega\rho_{f/s}c_{f/s} = 0 \tag{4.13}$$

Performing the inverse Fourier transform numerically as

$$T_0 = \frac{1}{2\pi}\iint_{-\infty}^{\infty}\widehat{T_0}(\xi_1,\xi_2)\exp[\mathrm{i}(\xi_1 x_1 + \xi_2 x_2)]d\xi_1 d\xi_2 \tag{4.14}$$

the surface temperature response in real space can be derived. The details of derivation can be found in Appendix B.

If all terms including heating laser power and distribution, optical reflectivity, R_{th}, α and film/substrate thermal conductivity anisotropy are defined accurately, the 3D model is capable to demonstrate precise transient-temperature-distribution all over the sample.

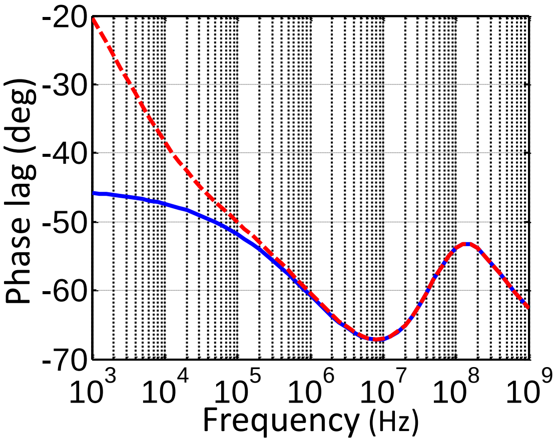

Figure 4.4 Phase-lag curves from the improved 1D model (blue line) and the 3D model (red dash line).

As stated previously, the 3D model can be used to validate assumptions of e_s measurement based on the 1D model and perform the sensitivity analysis. Fig. 4.4 shows the phase-lag curves of the 1D and 3D analytical solutions as a function of the frequency in the log scale. The radius of the heat-source area measured from experiment is used in 3D model, which is 10 μm. The other parameters used in the 3D model come from Table 4-1. The convergence trend of the phase-lag curves, with increasing frequency, displays the accomplishment of 1D heating in the high frequency region. At 1 MHz the phase-lag deviation (~0.5 degree) is found to be below the instrument noise level (~1 degree), sufficient to satisfy the 1D heating assumption. It confirms the statement of the 1D heating condition requirement: heating laser spot size should be at least 10 times larger than L_{th}.

4.2. Spatial-Domain Photothermal Reflectance Technique (SDPRT)

The causes of the phase lag in the frequency and spatial-domain measurements are different. In the spatial-domain measurements, the phase lag is generated from the separation of the heating and probe lasers. Depending on experimental conditions, one of the laser beams is scanned across sample surface while the other one is fixed. For laterally heterogeneous samples, scanning the heating laser requires solving the governing equations for each position. Therefore, it is preferable to move the probe laser and keep the heating laser stationary. If the sample surface reflectance condition is not uniform, to obtain a better signal-to-noise ratio, it is recommended to keep the probe laser at a highly reflective region and scan the heating laser.

The spatial-domain photothermal reflectance technique is essentially developed from the classic Angstrom's method. Thermal wave phase lag, $\Delta\varphi$, can be proved as a linear function of the distance between the heat source and the detection spot Δx:

$$\Delta\varphi = Re(q) \cdot \Delta x \tag{4.15}$$

where q is the thermal wave number, a function of modulation frequency and sample thermal properties. For a bulk sample (single layer without coating), the dispersion relation of q and thermal diffusivity, D, is:

$$q = \sqrt{i\omega/D} \tag{4.16}$$

The real part of q is

$$Re(q) = \sqrt{\omega/2D} \tag{4.17}$$

D can be extracted from the y-intercept of the dispersion relation curve on a log-log graph, with the slope of the phase lag – laser separation curve as the y-axis and the heating laser modulation frequency as the x-axis [8].

For layered samples, the dispersion relation becomes a function of the thermal properties of both layers and the thickness of the film. By assuming the film a good thermal conductor, thus no temperature gradient in the depth direction in the film layer, the governing equations are given as in Eq. (4.18) and (4.19) [37]

$$\rho_f c_f h \frac{\partial T_f}{\partial t} = k_f h \nabla_\perp^2 T_f + k_s \frac{\partial T_f}{\partial z} \tag{4.18}$$

$$\frac{\partial T_s}{\partial t} = D_s \nabla^2 T_s \tag{4.19}$$

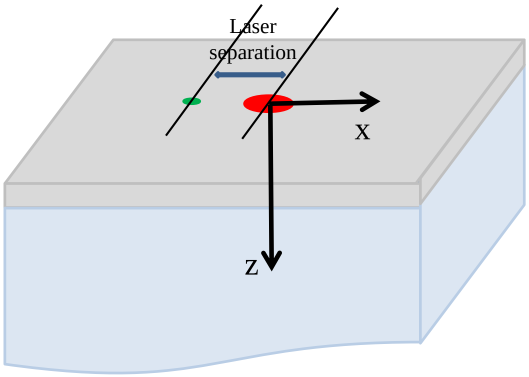

Figure 4.5 Spatial-domain measurement model and coordinate system.

where *x* presents the radius direction and *z* presents the depth direction. $\nabla_{\perp}^2 = \partial^2/\partial x^2 + \partial^2/\partial y^2$. The model and used coordinate system are plotted in Fig. 4.5.

By applying the method of separation of variables, *T=f(z)×exp(iqx-iωt)*, the dispersion relation can be derived as

$$q = \sqrt{\frac{i\omega}{D_f} + \frac{{q_0}^2}{2}[1 - \sqrt{1 - \frac{4i\omega}{D_s {q_0}^2}(1 - \frac{D_s}{D_f})}]} \tag{4.20}$$

where $q_0 = -\frac{k_s}{hk_f}$. More details can be found in ref. 37.

Similarly to Eq. (4.17), the "effective thermal diffusivity" of the layered sample can be defined to describe overall heat transport property as

$$Re(q) = \sqrt{\omega/2D_{eff}} \tag{4.21}$$

More mathematical work can be done on Eq. (4.20). By pushing *ω* to high or low frequency limitation, it is found that the real part of *q* becomes

$$Re(q) \approx Re(\sqrt{\frac{i\omega}{D_f} + \frac{{q_0}^2}{2}\left[-\frac{1}{2}\frac{4i\omega}{D_s {q_0}^2}\left(1 - \frac{D_s}{D_f}\right)\right]})$$

$$= Re(\sqrt{\frac{i\omega}{D_f} - \frac{i\omega}{D_s}\left(1 - \frac{D_s}{D_f}\right)})$$

$$\approx Re(\sqrt{\frac{i\omega}{D_s}}) = \sqrt{\frac{\omega}{2D_s}} \tag{4.22}$$

in low frequency region and

$$Re(q) \approx Re(\sqrt{\frac{i\omega}{D_f} + \frac{{q_0}^2}{2}\left[\sqrt{-\frac{4i\omega}{D_s {q_0}^2}\left(1 - \frac{D_s}{D_f}\right)}\right]})$$

$$\approx Re(\sqrt{\frac{i\omega}{D_f}}) = \sqrt{\frac{\omega}{2D_f}} \tag{4.23}$$

in high frequency region.

In both cases, *D* of one single layer can be extracted in a straight forward manner. Therefore, by modulating the heating laser frequency to very low or very high region, it is able to measure D_s or D_f separately. The overall dispersion relation (Eq. (4.20)) is plotted in Fig. 4.6 to validate this statement. The real part of q is dominated by D_s at low frequency end (i.e., below 10 Hz) and D_f at high frequency end (i.e., above 100 KHz) as in Eq. (4.22) and (4.23). In the transition region, both film and substrate properties have influences on q.

Physically this trend is caused by L_{th}. As introduced previously, L_{th} is the indicator of the thermal wave propagation range. In low frequency case where L_{th} is much larger than the film thickness, thermal wave penetrates deep into the substrate and the influence of film properties to the thermal wave propagation is negligible comparing to the substrate; with frequency increasing, L_{th} decreases and in the extreme case thermal wave cannot reach the substrate layer, thus the film properties dominates the thermal wave propagation.

The slopes of the simulated phase lag – lasers separation curves from the 3D model are plotted in Fig. 4.7 to inspect the assumption of the absence of a temperature gradient in the film. Although a noticeable deviation is found in the transition region, it does not break down the conclusion that q is dominated by D of only one layer in the extreme cases.

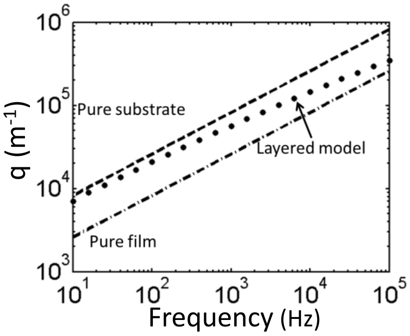

Figure 4.6 Dispersion relation curve of a layered sample [44]. (Dash line - substrate thermal diffusivity; dash-dot line – film thermal diffusivity; dot - real part of the thermal wave number)

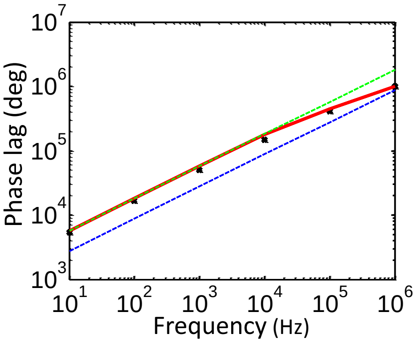

Figure 4.7 The comparison of thermal wave number obtained from the simplified model (red line) and the 3D model (black dot).

So far the strategy of measuring D_s and e_s from the spatial-domain and frequency-domain photothermal reflectance technique has been clarified. To optimize the measurement conditions and guarantee good measurement accuracy on the parameters of interest, a detailed sensitivity analysis is required.

4.3. Sensitivity Analysis

The sensitivity $S(\xi)$ is defined as below:

$$S(\xi) = \frac{\partial\varphi}{\partial ln\xi} = \frac{\varphi(\xi+\triangle\xi)-\varphi(\xi)}{\triangle\xi/\xi} \qquad (4.24)$$

where ξ is the parameter in question.

Except for the parameters of interest (D_s and e_s), other important ones are examined: thermal conductivity of the film, k_f, which is dependent on the film thickness due to microstructure effect and needs to be measured separately [51], heating laser spot size, which is important to validate the 1D heating condition, and R_{th}, which had been proved to influence e_s measurement result significantly. Hence, three thermal parameters k_s, D_s and k_f and the heating laser spot size in the spatial-domain measurement, and e_s and R_{th} in the 1D frequency-domain measurement are selected to be analyzed. Although the 3D frequency-domain measurements are not used to obtain any thermal properties, the sensitivity analysis is still applied on k_s, D_s, k_f, spot size and R_{th} to help better understand the influences of these parameters on the experiment.

Because the sensitivity analysis is planned to be performed before the real experiment, only approximated values of these parameters are used in this sensitivity analysis. k_f is expected to be half of the bulk values with the density and heat capacity not influenced by microstructure effect. It is a reasonable assumption if the films are fully dense [52]. In real experiments, the measurement is performed on two validation samples with different k_s that represent fresh and irradiated nuclear fuels. Correspondingly, in two simulation samples k_s and D_s are set as 10% and 80% of the film properties respectively. The properties used in simulation are listed in Table 4-2 (note the differences of k_f, D_f and h from Table 4-1).

The results of the sensitivity analysis are plotted in Fig. 4.8, 4.9 and 4.10. In Fig. 4.8(a), $S(\xi)$ is plotted for the spatial-domain measurement at a modulation frequency of 100 Hz for sample A. This plot illustrates that there is a relatively high sensitivity of D_s. This behavior is to be contrasted with the result at 50 KHz shown in Fig. 4.8(b). Without changing the sample, the sensitivity to k_f increases with modulation frequency and becomes larger than the other thermal parameters of the system. This sensitivity change with respect to frequency is essentially a restatement of the conclusion in Section 4.2 that q is mostly influenced by the substrate properties in low frequency region and film properties in high frequency region. Therefore, k_f and D_s

Table 4-2 The parameters used in the sensitivity analysis.

Parameters	Unit	Sample A	Sample B
k_f	W·m^{-1}·K^{-1}	11	
D_f	m^2/s	5×10^{-6}	
k_s	W·m^{-1}·K^{-1}	1.1	8.8
D_s	m^2/s	5×10^{-7}	4×10^{-6}
spot size SDPRT	μm	1	
spot size FDPRT	μm	15	
h	nm	200	
R_{th}	K·m^2/W	5×10^{-9}	
α	m^{-1}	6×10^{7}	

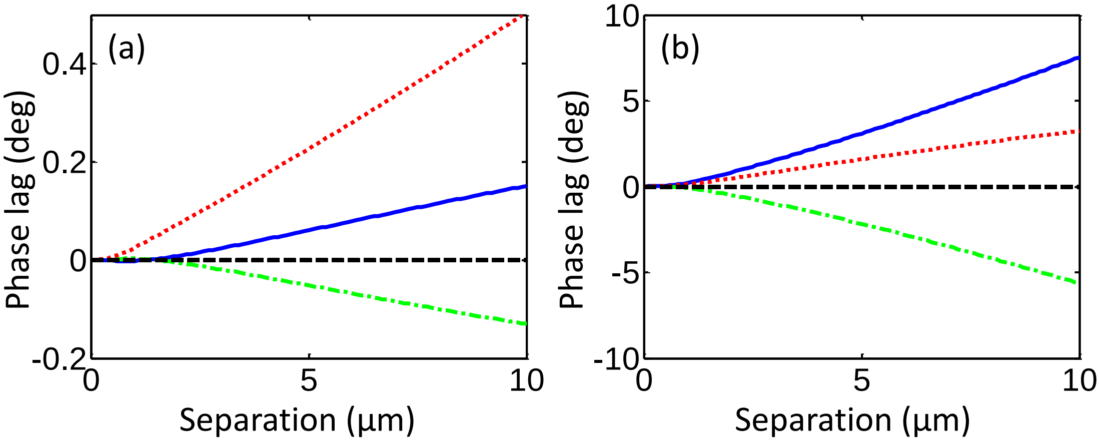

Figure 4.8 Sensitivity analysis of the spatial-domain measurement on sample A at the frequency of (a) 100 Hz and (b) 50 KHz (red dot – Ds, blue line – kf, green dash–dot line – ks).

measurements are decided to be performed at high and low frequencies respectively. It is worth noting that in both figures, the parameters of interest do not show dominant sensitivity thus an inverse fitting process is probably needed.

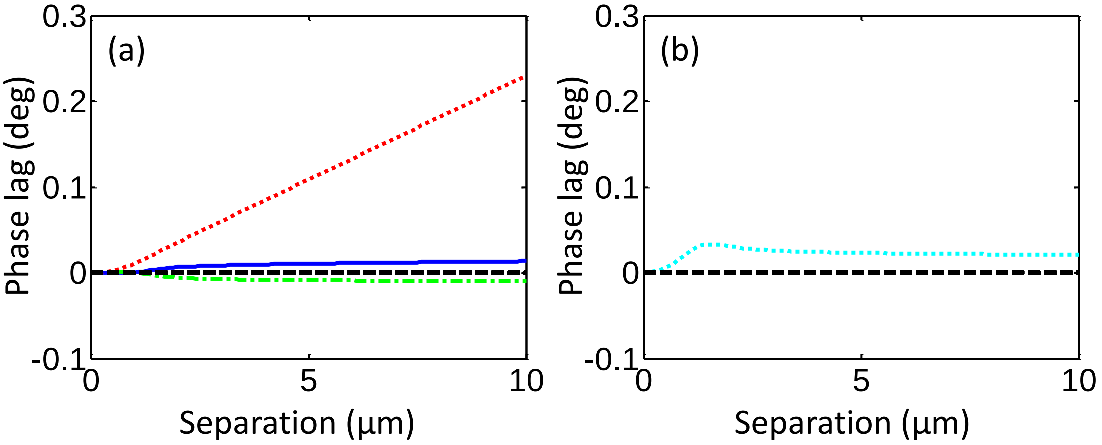

Figure 4.9 Sensitivity analysis of the spatial-domain measurement on sample B at 100 Hz(red dot – Ds, blue line – kf, green dash-dot line – ks, cyan dot – pump laser spot size).

In Fig. 4.9(a), $S(\xi)$ is plotted for the spatial-domain measurement at a modulation frequency of 100 Hz for sample B. A different situation here is that the sensitivity to D_s is an order of magnitude larger than the sensitivity to other parameters, which means a high confidence to get D_s on the sample with high k_s from the low frequency spatial-domain measurement thus the inverse fitting process is not required. The sensitivity of the pump laser spot size versus scan distance on sample B is considered in Fig. 4.9(b). The sensitivity changes sharply near the origin reflecting the finite spot size of the pump laser, and a constant offset is observed with increasing scan distance. A similar sensitivity curve is available on sample A, leading to the conclusion that the influence of this parameter is only near the origin thus it can be measured independently.

The sensitivity analysis in the frequency-domain measurements is shown in Fig. 4.10. The thermal parameters used here correspond to sample A. On sample B the situation is similar only the peak positions and magnitudes are different. Note that the treatment of R_{th} is different from the other parameters in Fig. 4.10. The approximated R_{th} from literature is believed to have an order of magnitude greater percentage-uncertainty than other parameters (i.e., R_{th} in real experiments may be found 50% different from the values in literatures, while for the other parameters the uncertainty is less than 10%). To help demonstrate the real influence of the parameters, the sensitivity curve of R_{th} is exaggerated by a ratio of 10. In Fig. 4.10(a), sensitivity to e_s and R_{th} are considered in the improved 1D model. As stated previously, the maximum of the sensitivity to these two parameters fall in the similar frequency region: the peak of e_s sensitivity is found in the range of 1-5 MHz, and the influence of R_{th} become noticeable in the range of 500 KHz – 20 MHz. In this range L_{th} is comparable to the film thickness, thus the boundary condition between the two layers, which contains both e_s and R_{th}, becomes significant.

The 3D frequency-domain measurement is considered last. In Fig. 4.10(b) each sensitivity curve has its own influence but no one is dominant. Theoretically, an inverse fitting process can be used to obtain each single parameter. However, low contrasts between sensitivity curves may become a problem if a high fitting accuracy is required.

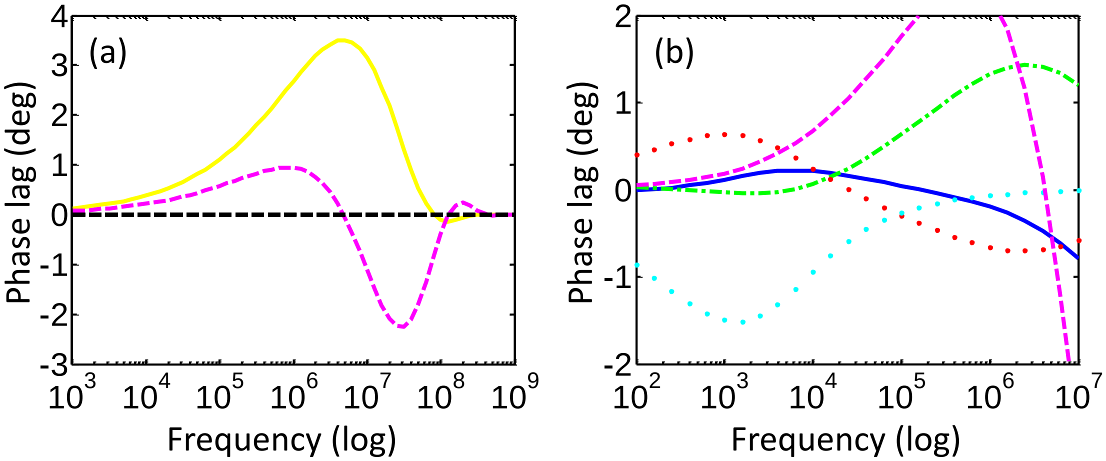

Figure 4.10 Sensitivity analysis of the frequency-domain measurement on sample B (red dot line – Ds, blue line – kf, green dash–dot line – ks, cyan dot – pump laser spot size, megenta dash line – Rth, yellow line – es).

CHAPTER 5

EXPERIMENT PROCEDURE

In this chapter, the preparation details of the experiment are given, which include two parts: design and build the experimental setup, and determine the reference sample and the samples of interest (validation samples). The experimental process is determined based on the results of the sensitivity analysis from Section 4.3.

5.1. Experimental Setup

The design diagram of the experimental setup is shown in Fig. 5.1. Two continuous-wave lasers with the wavelength of 532 nm (Coherent model Compass 315M) and 655 nm (lab built) are selected as the pump laser and probe laser, and the maximum powers are about 150 mW and 25 mW respectively. After passing through various optics, the laser intensity gets attenuated and the remaining power reaching the sample surface is only a few percentages of the output power. The measured values on the sample surface are 3 mW, 500 μW for the spatial-domain measurements and 5 mW, 700 μW for the 1D frequency-domain measurements (former ones are for the pump laser) approximately. An acousto-optic modulator (AOM, NEOS technologies model 23080 with the driver model N21080-1SAS) is used for the amplitude modulation of the heating laser, and the frequency is controlled by a function generator (Agilent Technologies model 33215A). To improve the probe laser quality, a pinhole-filter system composed of a pair of lens and a 50-nm pinhole is used. Scanning of the probe laser relative to the pump laser in the spatial-domain measurements is achieved by sending the probe laser to pass through a confocal lens pair. The first lens is mounted on a motorized stage (Newport model VP-25XA) with a mirror to make the probe laser beam to move on the x-y plane. The second lens converts the x-y motion of the beam into an angle change at the entrance of the objective lens. A 50X objective lens (Olympus model SLMPLN50X) is used in the spatial-domain measurement and the limit of the scan distance of this confocal system is approximately 100 μm. For the 1D frequency-domain measurements, to increase the heating laser spot size, a 10X objective lens (Olympus model LMPLFLN10X) is used instead. The pump laser is sent to the center of the objective lens using a dichroic mirror following the confocal system and the propagation vector is parallel to the objective-lens axis. The positions of the pump laser and probe laser on the sample surface are checked from a CCD camera (Panasonic model WV-BP140). The reflected probe beam is collected by a photo detector (New Focus nanosecond photo detector model 1621) and analyzed by lock-in amplifiers (Stanford Research System model SRS830 and SRS844) after passing a bandpass filter to block the pump laser beam.

One picture of our experimental setup is given in Fig. 5.2.

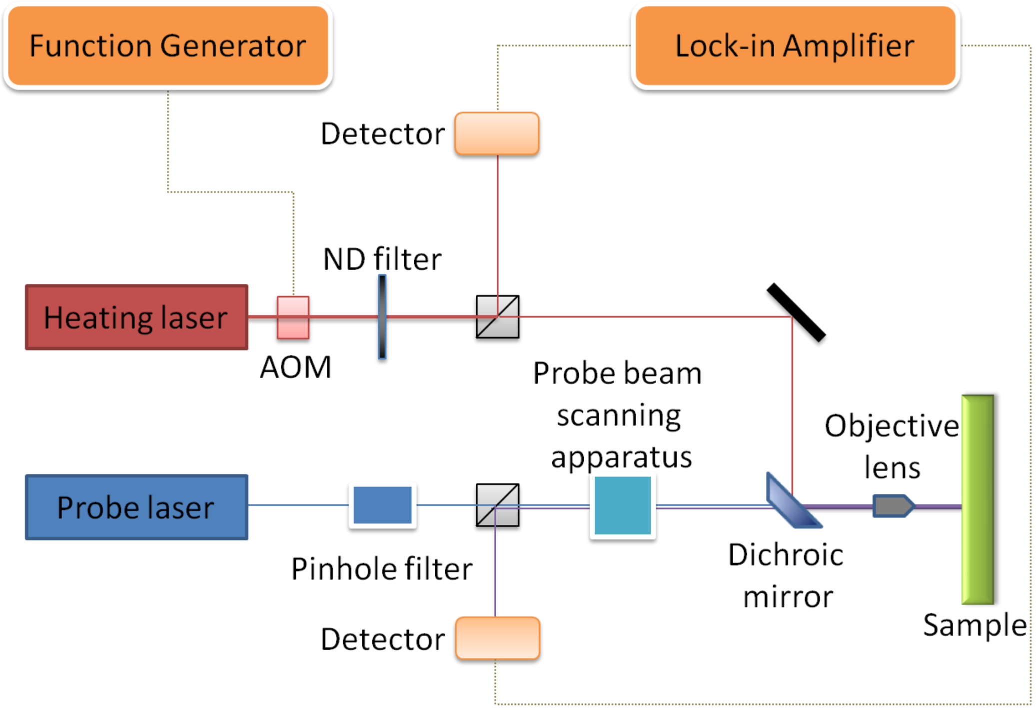

Figure 5.1 Design diagram of the experimental setup.

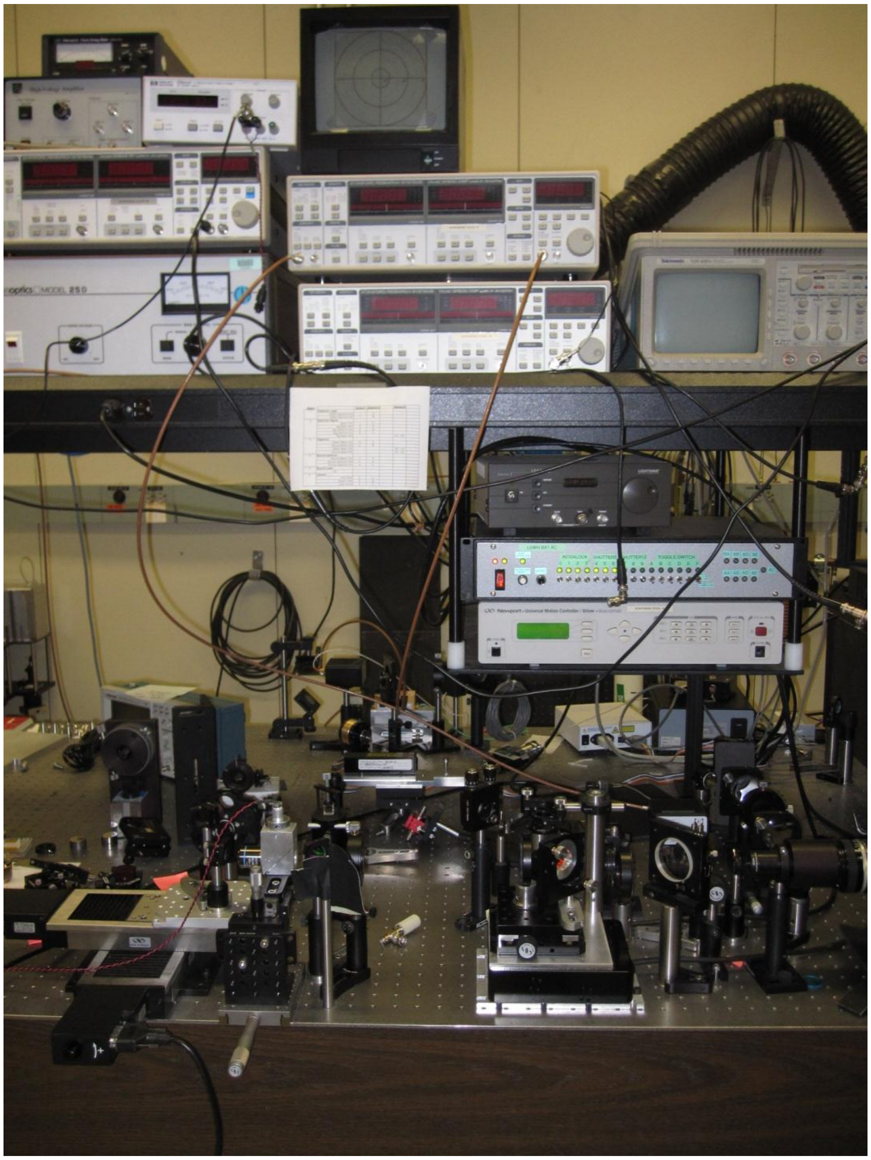

Figure 5.2 A picture of the experimental setup.

5.2. Sample Description

Two substrate materials are selected to validate the measurement setup. SiO_2 (Alfa Aesar quartz microscope slide, fused, $3.0 \times 1.0 \times 0.0394$ inch) has a thermal conductivity of 1.4 $W \cdot m^{-1} \cdot K^{-1}$, representing the highly burnt nuclear fuel, and CaF_2 (American Element Calcium Fluoride Windows, CA-F-02-WIN, 1 inch diameter) has a thermal conductivity of 9.2 $W \cdot m^{-1} \cdot K^{-1}$, representing the fresh nuclear fuel. As the reference sample to determine the thermal conductivity

Table 5-1 Information of the validation samples.

	SiO_2	CaF_2
k [W·m^{-1}·K^{-1}]	1.4	9.2
D [m^2/s]	9.5×10^{-7}	3.4×10^{-6}
e [J/(m^2·s^{½}·K)]	1436	4990
Vendor	Alfa Aesar	American Element
Production model	Quartz microscope slide, fused	Windows, CA-F-02-WIN
Size [inch]	3.0×1.0×0.0394	(Dia.) 1

of the film, k_f, a good thermal insulator is needed and we select SiO_2 as we had claimed before. Although both SiO_2 samples are from the same vendor, the measurements of the thermal conductivity of the substrate, k_s, from the validation SiO_2 sample and k_f from the reference SiO_2 sample are performed separately.

Titanium is selected as the coating material due to its good temperature coefficient of optical reflectivity (a parameter to describe optical reflectivity change due to temperature) at the probe laser wavelength. The coating films on two samples of interest and one reference sample are deposited simultaneously using thermal sputtering (ordered from Utah Nanofab, University of Utah). A thickness of 200 nm is suggested by sensitivity analysis. The exact film thickness is obtained from the picoseconds acoustic technique as 170 (±4) nm [53].

The details of the validation samples are summarized in Table 5-1.

5.3. Experimental Procedure

As stated previously, the diffusivity and effusivity of the substrate, D_s and e_s, are measured separately from the spatial-domain and frequency-domain measurements to extract k_s. In addition, due to the grain boundary scattering, k_f is different from the bulk value and has to be measured from the reference sample prior to the measurements of D_s and e_s. To ensure that the films on all samples have the same coating condition (then the thermal properties and thickness of the film can be considered as identical), the reference sample and samples of interest must be prepared simultaneously.

The recipe to evaluate k_s is composed of three steps: measuring k_f, D_s and e_s. An outline of the approach is given below:

1) measure thermal conductivity of the film (k_f)

Fig. 4.8(b) in the sensitivity analysis section demonstrates that the spatial-domain measurement in high frequency is proper to get k_f, and an inverse fitting process is required. As mentioned previously, spot size and k_f generally affect different parts of the phase-lag profile: spot size only affects the area near the heat source where other thermal properties including k_f have very low sensitivity. Hence the two parameters can essentially be obtained independently from each other. It is worth noting that, because the thermal wave propagation attenuates exponentially with frequency, the high-end limit of the heating laser frequency of the spatial-domain measurements exists and it is always below 1 MHz (100 KHz in this project), not enough to reach the linear region of the dispersion relation diagram on the log-log graph (e.g., Fig. 4.6) to get D_f and then extract k_f.

With the consideration of both sensitivity and signal quality, the experimental data to fit k_f are from 5-KHz, 10-KHz and 50-KHz spatial-domain measurements.

2) measure thermal diffusivity of the substrate (D_s)

The spatial-domain measurements are carried out in low frequency region to get D_s from the samples of interest. After plotting the dispersion relation diagram on a log-log graph, we can envision two scenarios: a) a linear region is observed at low frequencies, indicating that we are only sensing the substrate, or b) a linear region is not reached with decreasing frequency. The same issue of k_f measurements exists here as well. In principle the linear region is always available if the heating laser frequency is below a critical value. However, in real experiments, there is a low frequency limit determined by the signal-to-noise ratio. In this project the low frequency limit is in the range of 10-100 Hz depending on the substrate sample.

In case a), D_s can be obtained from the position of the linear region with high confidence. In case b), the inverse fitting process is necessary with D_s, k_s and spot size as the fitting parameters. The data of spatial-domain measurements at 100 Hz, 500 Hz, and 1 KHz are selected for the inverse fitting process. Due to the complication of the inverse fitting process and the issue of the solution uniqueness, case b) should always be avoided if possible.

3) measure thermal effusivity of the substrate (e_s)

The key relation to improve e_s measurement accuracy is that the heating laser spot size is at least 10 times larger than the thermal diffusion length which is comparable to the film thickness. This relation ensures 1D heating and a good sensitivity to measure e_s. However, enlarging the heating laser spot will decrease the power density and reduce the signal intensity. Thus a balance is needed between the 1D heating condition and signal quality which depends on the experimental conditions. Based on the suggested 200-nm film thickness, we decide to modulate the heating laser frequency to 1 MHz, and adjust the spot size to ~ 10 µm.

Table 5-2 Optimized parameters from the sensitivity analysis.

Optimized Terms	Values
Frequencies for k_f extraction	5 KHz, 10 KHz, 50 KHz
Frequencies for D_s extraction	100 Hz – 100 KHz, at least 10 different frequencies; 100 Hz, 500 Hz, 1 KHz if the inverse fitting process is needed
Frequency for e_s extraction	1 MHz
Film thickness	200 nm
Heating laser spot size in e_s measurement	≥10 µm

Within the 1D case, e_s can be calculated either from a fixed-frequency measurement or a frequency-domain scan. It is always recommended to examine the 1D heating condition by comparing the phase profile from the 1D frequency-domain scan and the 3D analytical solution with fitted value of e_s.

All the optimized experiment parameters are summarized in Table 5-2.

CHAPTER 6

EXPERIMENTAL RESULTS AND DISCUSSION

In this chapter, the experimental results are given. All steps generally follow the recipe we stated in Section 5.3: the spatial-domain measurements are applied in high frequency region on the reference sample to get the thermal conductivity of the film, k_f; then the fitted k_f is used to get the substrate thermal diffusivity, D_s, of the samples of interest from the spatial-domain measurements in low frequency region, and thermal effusivity, e_s, from the 1D frequency-domain measurements; eventually substrate thermal conductivity, k_s, is calculated from D_s and e_s and compared with the data supplied by vendors. The sources of experimental errors are analyzed. Quantitative uncertainty analysis is carried out in the end of this chapter.

6.1. The Determination of Film Thermal Conductivity (k_f)

Suggested by the sensitivity analysis, the spatial-domain measurements are carried out in the high frequency region (5 KHz, 10 KHz, and 50 KHz) to extract k_f. Scan distance of the spatial-domain measurements is 8 μm for the 40-spot scan and 12 μm for the 60-spot scan, ensuring the spatial resolution of 0.2 μm between neighboring spots. The 60-spot scan is always recommended because the sensitivity of the parameters of interest is higher at the ends of phase-lag curves. In case of the sample surface having a poor reflectance condition, the signal can be very noisy at the ends and the 40-spot scan becomes the better choice. A 50X long-working-distance objective lens is used to focus lasers and get higher resolution. Both heating and probe laser beams have a size of several millimeters before been focused and 1 – 1.5 μm on the sample surface after.

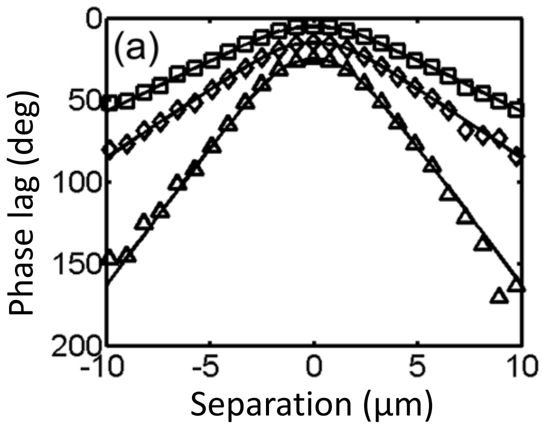

Figure 6.1 An example of the spatial-domain measurement data for kf extraction [44].

The measurements are taken on the reference sample repeatedly to decrease the random errors. After a data refinement (details are given in next section), good data are collected to get k_f. One example of good experimental data is given in Fig. 6.1 with least square fit curves from the 3D model introduced in Section 4.1.3, and the best fit value of k_f is 9.6 $W{\cdot}m^{-1}{\cdot}K^{-1}$. It is significantly lower than the literature value of the Ti bulk, 21.9 $W{\cdot}m^{-1}{\cdot}K^{-1}$. The over 50% deduction of the thermal conductivity matches other published result on thin film study [54].

6.2. Data Refinement for Film Thermal Conductivity (k_f)

Due to the inhomogeneity of the film and substrate layers and the previously mentioned sensitivity issues in the inverse fitting process, a significant variability in the fitted value of k_f is found even for the data sets that appear similar. It will lead to an uncertainty problem in the e_s measurement and k_s extraction if the variability is not taken care of. A simple way to solve it is to take a large number of scans at each frequency. It can statistically lower the random error in the measurement and narrow the fitting parameter uncertainty. Some more treatments stated in this section will help the refinement and guarantee a reliability of the fitted k_f value.

1) Determine the Symmetry Parameter and filter out asymmetric data

The phase-lag curves from the spatial-domain measurements are theoretically symmetric with the assumption that the sample is isotropic and homogeneous. The curves generated from the simulation program also display symmetry representing perfect experimental conditions and sample structure. However, in real experiments, several factors may cause asymmetry data, which may significantly influence the fitting result quality. The common possibilities include: the sample is not aligned perpendicularly to the laser beams; the intensity of the probe/heating laser either is not consistent or does not have a Gaussian distribution; the sample surface is poorly coated/polished or has defects/oxidation which leads to variations in reflectivity; or the instruments generate electronic noise. It can be seen that some of the reasons, such as the oxidation of the metal film, are inevitable in the real experiment. Fig. 6.2 and 6.3 give some examples of the experimental data set with poor symmetry.

The first step of the refinement is to check the data symmetry and take off some sets before the inverse fitting process. To quantitatively compare the symmetry conditions among all sets of data, we define a Symmetry Parameter (SP) step by step as below:

Pre-treatments: comparing the first half of the phase-lag data (which represents the left side of the phase-lag curve) to the second half (which represents the right side of the phase-lag curve) point by point, normalize the phase-lag differences from each point pair (1st and nth point, 2nd and (n-1)th point…) to balance the magnitude differences of the phase lag across various of frequencies. A few pairs of points (two pairs for 40-spot data and three pairs for 60-spot data) with large differences are taken off from the data set so that random noise does not influence the overall symmetry evaluation.

Obtaining necessary slope parameters from experimental data: two slopes are extracted for one side of each phase-lag curve (totally four slopes are obtained from one curve): from all useable points and from the points only on the ridges. Generally, the “useable points” only exclude the data on the top of the phase-lag curve which is mostly sensitive to the heating laser spot size but not material properties; and the “ridge points” exclude the data on the top of the phase-lag curve and the data at both ends (always noisy). For instance, for the sets of 60-spot scan data, the slopes covering all “useful points” on each side use the 1st to the 25th point, and the 35th to the 60th point; the slopes fitted from the “ridge points” use the 5th to the 20th point, and the 40th to the 55th point. The points on the top (from 25th to the 35th point) are always not used. The reason of taking two slopes from the same side is to consider both the ridge points with good signal-to-noise ratio and the useful points with good sensitivity.

Defining General Slope, Symmetry Parameter and Overall Symmetry Parameter: three more parameters are defined to describe the overall symmetry conditions quantitatively. General Slope (GS) is defined as the square root of the product of the two slopes on the same side; and SP is defined as the ratio of two GSs from each side of a scan curve, while the larger GS is always placed in the numerator of the expression, i.e., SP $\geq$ 1. The last one, Overall Symmetry Parameter, (OSP) is defined as OSP = (SP1+SP2+SP3) * max (SP1,2,3).

These definitions are necessary and useful. GS considers the balance of a good signal-to-noise ratio and the sensitivity of the thermal property of interest; SP gives a single indicator of the symmetry condition of a phase-lag curve; and OSP is the overall evaluation of the symmetry condition of an experimental data set. The definition of OSP also takes a complicated case into consideration. The data with three sufficient SPs are preferred to the data with only two excellent SPs. Current definition of OSP can successfully avoid the improper selections.

Setting OSP filter to separate out data with poor symmetry: in ideal case, all single SPs equal to 1 and the OSP = 3. For real cases, a value of SP less than 1.1 is considered acceptable. The critical value of the OSP filter is set 3.4 for 40-spot scans and 3.5 for 60-spot scans. The data with a large OSP is rejected from entering next filter.

2) Fit the data and get the Deviation Parameter

In the inverse fitting process, a "fitting quality indicator" is required to describe the deviation between the fitting curve and the experimental one. The sets of data with bad fitting quality will be filtered out from the final step, k_f extraction. In this refinement this indication, Deviation Parameter (DP), is defined with the steps below:

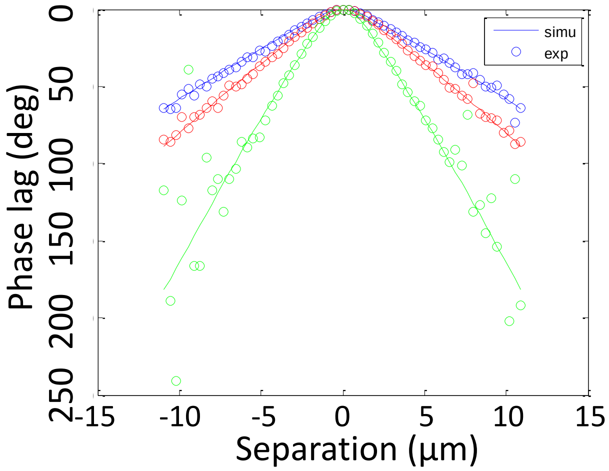

Figure 6.2 An example of a 60-spot data set with unacceptable asymmetry. Notice the significant scatter of the data measured at 50 kHz (the green data set).

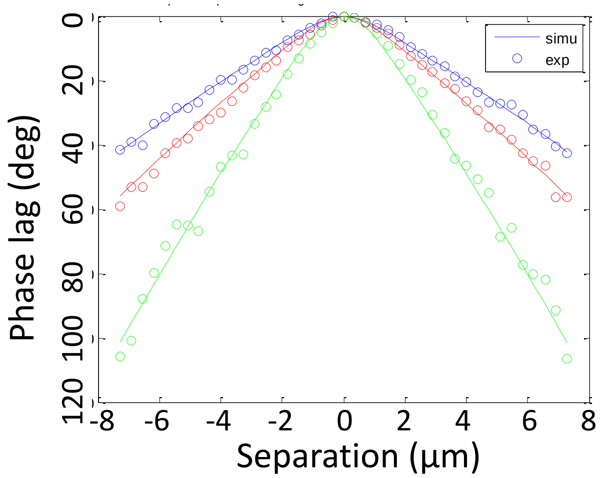

Figure 6.3 An example of a different type of asymmetric data set. The measured data at 50 KHz is shifted to the right relative to the fitted curve.

Pre-treatments: as we stated previously, the data at the ends of each side has good sensitivity to k_f but low signal-to-noise ratio. To help decrease the noise influence and keep useful part of the data, we determine to weight the individual deviations between the fitting curve and the experimental phase-lag spots by weight factors before the deviations get summed up. The weigh factors change from 1 to 0.2 depending on the signal-to-noise ratio (or signal intensity).

Defining Deviation Parameter: after all the deviation summations of single phase-lag curves are obtained, the average deviations at three scan frequencies are calculated. DP of each single curve is then defined as the ratio of the individual deviation summation to the average deviation at corresponding scan frequency. A value of DP = 0 indicates a perfect fit quality, and DP = 1 indicates an averaged fit quality. The reason why the average deviation is involved here is to make DP an independent parameter of the number of spots, scan sets, and overall data/fitting quality. With current definition, even if all experimental data are noisy, it is still able to select sufficient relatively good data to extract k_f.

Defining Overall Deviation Parameter and setting the ODP filter: similar to OSP, an Overall Deviation Parameter (ODP) is required to describe the overall deviations of a set of data. It is defined following OSP as ODP = (DP1+DP2+DP3) * max (DP1,2,3). An ODP $\leq$ 4 is considered acceptable (for both 40-spot scan and 60-spot scan data).

See Fig. 6.4 for a comparison of unacceptable and acceptable data. Note how insignificant the differences appear to casual observation. Without the rigor of the data vetting process, it would not be possible to separate accurate data from scatter. Only data that meets both OSP and ODP criteria should be picked to extract k_f.

3) Extract k_f from the vetted data

In real experiments, about 40% of data that pass both OSP and ODP tests can be selected to extract k_f. Two common statistical treatments, the mean or mode, were not selected in this project. A more complex, but also more reliable, method was designed by using a chart of

OSP/ODP (or a function of both) versus fitted k_f. Ideally, the values of k_f fitted from the data passing both filters fall in a small range. The data points away from this range should be taken off. The data before and after refinement are plotted in Fig. 6.5 with this design. An irregular fitting result on the left is found and filtered out, displaying the advantage of this design compared to the common statistic methods.

The power of the refinement is seen that the variation of the fitted k_f decreases from 60% before the refinement to 25% after it, and the uncertainty is well controlled in 10%.

6.3. The Determination of Substrate Thermal Diffusivity (*D_s*)

The experimental data of SiO_2 and CaF_2 samples are plotted in Fig. 6.6. D_s is determined to be 9.8×10^{-7} m^2/s of the SiO_2 sample from the linear region of the dispersion relation curve in the frequency range of 20 Hz – 100 Hz with a slope of $\Delta\log(\mathrm{real}(q))/\Delta\log(\omega)=0.475$ (mentioned in Section 5.3). In an ideal case the slope equals to 0.5. For the CaF_2 sample, the linear region covers a larger frequency range of 1 KHz to 100 KHz and the slope of $\Delta\log(\mathrm{real}(q))/\Delta\log(\omega)=0.498$ and D_s is determined as 3.25×10^{-6} m^2/s. Based on the forms of the curves in the figures and the slope values of the linear region (0.475 for SiO_2 and 0.498 for CaF_2), D_s measurement on the CaF_2 sample has a higher reliability.

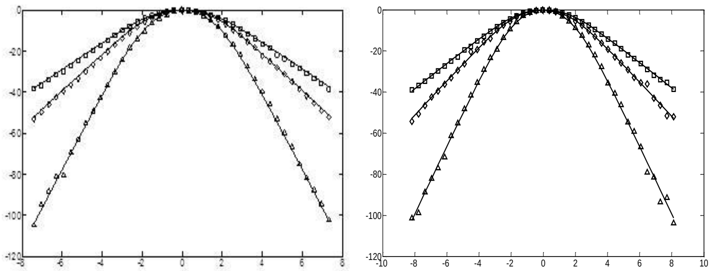

Figure 6.4 A comparison of two fitting results. On the left: Good fitting at high frequency and poor fitting at low frequency (the whole fitting curve is above the experimental data). On the right: Acceptable fitting at all frequencies. The right data set has better fitting quality, i.e., a smaller ODP value (x-axis: separation [μm], y-axis: phase lead [deg]).

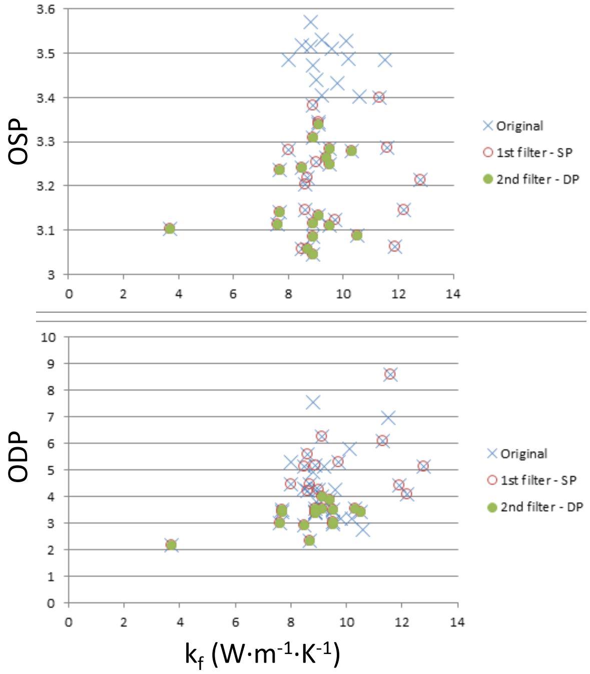

Figure 6.5 Refinement result (overall). Upper pane: OSP vs. kf. Lower pane: ODP vs. kf. Note that the data with large OSP and ODP values also have large deviations in the value of kf. Values of kf which passed both filters generally fall in the range of 8-10. An outlier is found on the left part of the lower chart at $k_f \approx 4$.

6.4. The Determination of Substrate Thermal Effusivity (e_s)

The 1D frequency-domain measurements at 1 MHz are performed to get the phase lag to extract e_s. In the experimental setup, we replace the 50X objective lens by a 10X objective lens to enlarge the heating area. The radius of the heating laser beam spot, which has a Gaussian profile, is measured to be 8-15 μm (about 10 times larger than 1-1.5 μm with the 50X objective lens). The thermal diffusion length, L_{th}, of Ti film at 1 MHz is about 1 μm. So the ratio of heating laser spot radius to L_{th} is about 10, which satisfies the 1D heating criterion.

The phase lags of the fixed-frequency measurements are 60.4 degree for SiO_2 and 46.3 degree for CaF_2. As stated previously, the thermal contact resistance, R_{th}, and optical absorption coefficient, α, are obtained from the literatures and the values are 5×10^{-9} Km^2/W and 6×10^{7} m^{-1}

respectively. e_s of SiO_2 and CaF_2 substrates are determined to be 1475 J/($m^2s^{½}$K) and 4300 J/($m^2s^{½}$K), respectively, from the equations in Section 4.1.2.

6.5. Thermal Conductivity (k_s) Extraction and Discussion on Experimental Errors

Based on the e_s and D_s measured in the former sections, k_s of SiO_2 and CaF_2 are calculated to be 1.44 $W \cdot m^{-1} \cdot K^{-1}$ and 7.75 $W \cdot m^{-1} \cdot K^{-1}$, respectively. All the measured thermal properties are listed with the literature values in Table 6-1.

Comparing to the 3% error of the measured k_s of SiO_2, the CaF_2 sample has a relatively large error of 16%. The larger experimental error on CaF_2 sample could be from several sources. One important reason is that k_s of CaF_2 is strongly depending on the temperature [55]. The temperature rise in the experiment due to laser focusing is approximately 10-50 K, which can lead to up to 10% descent of k_s. The sources of the experimental errors are discussed in next sections. The quantitative uncertainty analysis is given in Section 6.6, including the individual uncertainties of the D_s and e_s measurements and the overall uncertainty of k_s extraction.

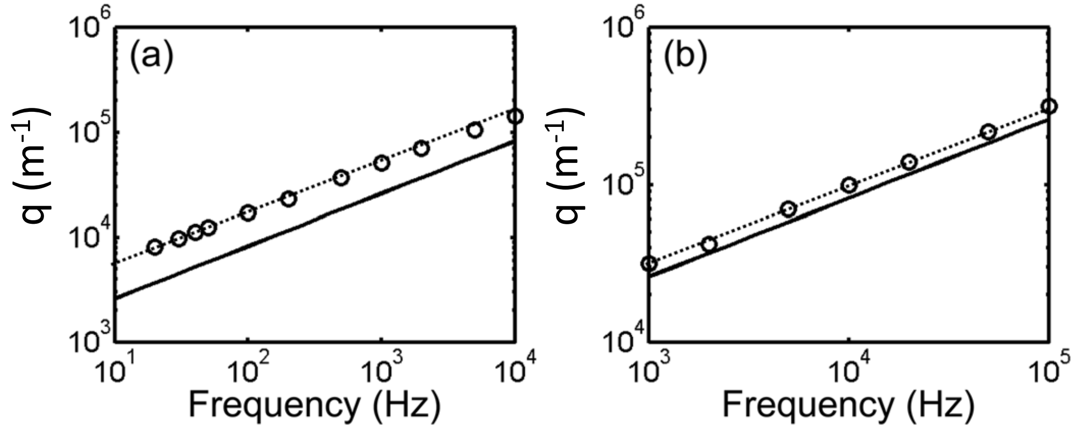

Figure 6.6 Dispersion relation plots from the real experimental data of SiO2 and CaF2 samples [44].

Table 6-1 Measured thermal properties and the literature values of the validation samples.

Parameters	**unit**	**SiO_2**	**CaF_2**
Phase lag	degree	60.4	46.3
e_s, measured	$J/(m^2 s^{½} K)$	1475	4300
e_s, literature	$J/(m^2 s^{½} K)$	1436	4990
e_s error		3%	-14%
D_s, measured	m^2/s	9.8×10^{-7}	3.25×10^{-6}
D_s, literature	m^2/s	9.5×10^{-7}	3.4×10^{-6}
D_s error		3%	-4%
k_s, measured	$W \cdot m^{-1} \cdot K^{-1}$	1.44	7.75
k_s, literature	$W \cdot m^{-1} \cdot K^{-1}$	1.4	9.2
k_s error		3%	-16%

6.5.1. Discussion of Substrate Thermal Diffusivity (D_s) Measurement

The measured D_s of both the SiO_2 sample and CaF_2 sample showed agreement to the literature values with less than 5% error. It is not surprising for numerous reasons:

First, each scan in the spatial-domain measurement covers a distance of 20 μm. As concluded previously, the phase lags from the area covered by or close to the heat source do not have sensitivity to extract D_s. Comparing to the heat source area which is smaller than 3 μm, the large scan distance guarantees enough useful data in phase-lag profile for D_s extraction.

Second, each phase-lag profile is composed of at least 40 data spots. Inevitably, a few points will be of poor quality, but statistically they have little impact on the fitting process. Poor data points can be caused by imperfections in the film such as local variations of optical. Additionally, the quality of the laser plays a role, as small instabilities can also affect the measurement. In any case, with careful control, the overall data has sufficient quality to extract D_s with high confidence.

The most important reason is that D_s values are extracted from the linear region of the dispersion relation but not from the inverse fitting process. In our experiment, 5-10 sets of spatial-domain measurements at different frequencies were performed to get D_s. It significantly improved the measurement reliability even if one or several sets of data do not have good signal-to-noise ratio thus the slope (real part of thermal wave number) cannot be determined correctly. For example, in Fig. 6.6 (b), the thermal wave number obtained at 2 KHz (second from left) is obviously below the fitted straight line representative of D_s, but other data points help maintain experimental reliability.

6.5.2. Discussion of Substrate Thermal Effusivity (e_s) Measurement

Some treatments were carried out to improve the data quality in e_s measurement: a time constant of 10 s was set in the lock-in amplifier comparing to 300 ms or 1 s in the spatial-domain measurement (longer time-constants can effectively decrease the data variation and improve the signal-to-noise ratio); and the experimental data was averaged from 150 or 200 phase-lag values to decrease the random error. However, the measured e_s of CaF_2 still showed a relatively large deviation from the literature value.

The primary reason for the large error in measurement of CaF_2 is the breakdown of the 1D heating assumption for higher conductivity samples. This effect is shown by the uncertainty quantification in Section 6.6. In order to assure 1D heating in e_s measurement, L_{th} should be always guaranteed to be smaller than one-tenth of the heating laser spot size. On the layered sample, the effective thermal diffusion length, $L_{th,eff}$ (a complex function of the thermal properties of both layers, calculated from effective thermal diffusivity, D_{eff}, defined in Eq. (4.21)) should be used instead. The higher value of D_s of the CaF_2 substrate (3.4×10^{-6} m^2/s for CaF_2 vs. 9.5×10^{-7} m^2/s for SiO_2) leads to larger D_{eff} and $L_{th,eff}$, causing increased phase-lag deviation between the 1D and 3D model. Additionally, larger D_{eff} also allows more heat dissipation lowering the signal intensity.

In order to improve it, a ratio of 10 between the heating laser spot size and $L_{th,eff}$ should be guaranteed, which means either the heating laser spot size should be increased, or the measurement should be performed at higher frequency. For the current setup, the modulation frequency and laser spot size are restricted by the heating laser being used. To overcome these limitations and reduce experimental error caused by the breakdown of the 1D heating condition, the recommendation is to replace the heating laser with one of higher power.

The shape, intensity distribution, and relative position of the heating and probe laser may also cause measurement error. In the 1D model, the heat source and the probe are described as two points. However in reality, they are laser beams with Gaussian distributions of intensity. A numerical model built in COMSOL Multiphysics (introduced in Chapter 7) proves that, if both lasers are perfectly concentric, the deviation caused by laser area and distribution is negligible. On the other hand, even a 1-μm offset between the laser centers can lead to several-degrees of phase-lag deviation, and thus, significant experimental error. In this setup, the heating laser is fixed and the probe laser is scanned by the motorized stage. The concentric position is found when the reflected probe beam intensity reaches maximum. If the intensity of the probe laser does not have a good Gaussian distribution, the concentric position may not be found correctly and the experimental error will be generated from the laser beams offset. A poor distribution with multiple random spikes had been found on the intensity distribution of the probe laser used in this system. A pinhole filter system composed of a pair of lenses and a 50-nm pinhole aperture was added to fix it.

6.6. Uncertainty Quantification

After the sources of experimental error are analyzed qualitatively, an uncertainty quantification to show the influences of all parameters and errors on the experimental result (mainly in e_s measurement) is performed.

6.6.1. Uncertainty Analysis in Substrate Thermal Diffusivity (D_s) Measurement

There are two types of experimental errors. One is systematic error that is a consistent bias in measurement. It only influences the results into one direction and can be decreased or even eliminated if the causes are identified and proper treatments are done. The other type is random error. It is caused by inherently unpredictable fluctuations in the readings from the measurement instruments. It can be reduced by applying the measurements repeatedly, but hardly eliminated.

The systematic error in D_s measurement generally comes from two main sources. The more important one is that the value of D_s may not be extracted from the perfect linear region of the dispersion relation. In other words, the measurement frequency is not low enough and the film properties still influence the thermal wave number. Due to the existence of the low frequency limit, only the inverse fitting process can decrease the systematic error in this case. Another possible source is from an experimental parameter called magnification factor. It is used to describe the ratio of the probe laser beam scan distance on the sample surface to the movement of the motorized stage. Magnification factor is 1 μm/μm if there is no lens used in the system, which means 1 μm movement of the probe laser on the motorized stage leads to 1 μm displacement of the laser spot on the sample. In our setup, the probe laser beam passes the objective lens and the confocal system before it reaches the sample surface and the magnification factor is no longer 1 μm/μm. After repeated measurements, with the 50X objective-lens, the magnification factor was determined to be 0.0368 mm/mm, or 36.8 μm/mm. It is worth noting that any movement of optics in the experimental setup may lead to a different magnification factor. The error of the magnification factor determination causes the error of the phase-lag profile slope, and ultimately the systematic error of D_s measurement. Measuring magnification factor repeatedly with precise motorized stage can effectively decrease this error. In our experiment, the curve slope in the linear region of dispersion relation had been checked, and the magnification factor was measured with a high confidence. Therefore, systematic error in D_s measurement is believed to be trivial.

The random error in D_s measurement is from the determination of D_s after the dispersion relation is plotted on the log-log graph. Increasing the numbers of experimental data sets can effectively control this random error to less than 5%. Due to the errors obtained on the SiO_2 samples and CaF_2 samples having opposite signs (+3% for the SiO_2 sample and -4% for the CaF_2 sample), it is believed that the overall experimental error in D_s measurement is dominated by the random error.

6.6.2. Uncertainty Analysis in Substrate Thermal Effusivity (e_s) Measurement

The possible sources of the experimental error in the e_s measurement have been discussed in Section 6.5.2. Because the phase-lag values do not change linearly with most parameters, the percentage uncertainty on different samples should be calculated separately. In this section, the quantitative analysis is given on the CaF_2 sample which has a relatively higher experimental error.

In the improved 1D model, which we built for the e_s measurement, several parameters may lead to the experimental error, including the film properties (film thickness, k_f, and α), R_{th}, the phase-lag deviation between the theoretical model with 1D heating and experiment with 3D heating, and instruments. The individual uncertainties of these parameters are listed below:

1) Film thickness. The thickness of the Ti film was measured by the picoseconds acoustic technique. 25 sets of data are analyzed and the film thickness was determined as 170 nm with an uncertainty of 2%.
2) k_f scattering. To control the data scattering, a refinement had been applied on the original experimental result of the k_f measurement. The details had been given in Section 6.2, and the uncertainty after the refinement was controlled to be 7-10%. A mid number of 8% is used in the uncertainty analysis.
3) R_{th} and α. The approximated values of R_{th} and α from literatures are used in the fitting program. The differences between the literature values and the real ones can cause experimental error. On R_{th}, which strongly depends on the local adhesive conditions, a reasonable guess of the percentage uncertainty is 50%. For α, it is assumed to be 5%.
4) 1D/3D model deviation and instruments. The uncertainty of the measured phase lag from the lock-in amplifier is observed to be 1 degree, with the deviation of the assumed 1D heating condition and the real 3D heating condition, which is approximately 0.5 degree. For the CaF_2 sample, the percentage uncertainties from the instrument and 1D/3D heating condition are 7.2% and 3.7%, respectively.

The individual uncertainties and the corresponding contributions to the overall uncertainty are listed in Table 6-2.

The overall uncertainty of the e_s measurement can be calculated from Eq. (6.1) below and the value is 9.3%:

$$\left(\frac{U_{e_s}}{e_s}\right)^2 = \sum\left[\left(\frac{\varphi}{e_s}\right)\frac{\partial e_s}{\partial \varphi}\frac{U_\varphi}{\varphi}\right]^2 \tag{6.1}$$

Table 6-2 Summary of the individual uncertainties of all experimental parameters and their contributions to the overall uncertainty.

CaF_2	Individual uncertainty	Contribution to overall uncertainty
Film thickness	2%	0.3%
k_f	8%	2.8%
α	5%	0.2%
R_{th}	50%	3.5%
Instrumental	1 deg	7.2%
1D/3D heating	0.5 deg	3.7%

where φ represents the variables in the table.

The uncertainty of k_s is propagated from D_s and e_s measurements, and from the same Eq. (6.1), it is calculated to be 9.6%. Considering that the k_s shift from temperature rise is about 10%, the overall measurement error of the CaF_2 sample (16%) is acceptable.

6.7. Exploration of Measurement Range

Samples with significantly different values of k_s have been tested with this setup without specific system optimization and the results are listed in Table 6-3. The experimental results show agreement (errors within 20%) on the samples with k_s less than 10 $W \cdot m^{-1} \cdot K^{-1}$ such as glassy carbon (GC) and ZrO_2. It again proves the capability of this setup to measure k of nuclear fuels. On the other hand, the experimental errors for high thermal conductivity samples, such as Chromium and Zirconium, are relatively large (30%-40%), because the measurement system is optimized for materials with thermal conductivity < 10 $W \cdot m^{-1} \cdot K^{-1}$. The measurement system could be optimized for higher conductivity samples to increase measurement accuracy if needed.

Table 6-3 Experimental results on more samples.

	Parameter, Units	**Measured**	**Literature**	**error**
ZrO2	D, mm^2/s	8.7×10^{-7}	8.7×10^{-7}	0%
	e, J/(m^{2}Ks$^{0.5}$)	1980	2144	8%
	k, W·m^{-1}·K^{-1}	1.85	2	7%
GC	D, mm^2/s	5.4×10^{-6}	5.1×10^{-6}	6%
	e, J/(m^{2}Ks$^{0.5}$)	2200	2800	21%
	k, W·m^{-1}·K^{-1}	5.1	6.3	19%
Zr	D, mm^2/s	8.5×10^{-6}	12.5×10^{-6}	32%
	e, J/(m^{2}Ks$^{0.5}$)	4550	6400	29%
	k, W·m^{-1}·K^{-1}	13.3	22.6	41%
Cr	D, mm^2/s	2×10^{-5}	2.94×10^{-5}	32%
	e, J/(m^{2}Ks$^{0.5}$)	13500	17350	22%
	k, W·m^{-1}·K^{-1}	60.4	93.9	35%

CHAPTER 7

COMPUTATIONAL SIMULATION

COMSOL Multiphysics (shorten as “COMSOL” below) is a finite element analysis software for the modeling and simulation of various physics and engineering applications. To check the influences of some experimental parameters which are not possible to be considered in the analytical models, such as probe laser distribution and temperature dependence of thermal conductivity, a numerical model is built and analyzed using COMSOL. To validate the numerical model, the simulation results are compared with the analytical solutions first. After a good agreement is reached, the parametric analysis is done to guide the experiment.

7.1. Introduction of Numerical Model

The material properties and boundary conditions of the analytical models in Table 4-1 are also used in the numerical model. Due to the symmetric character of the homogeneous sample and the heat source boundary conditions, the 3D numerical model can be accurately modeled by the 2D axisymmetric coordinates. It can significantly lower the computer hardware requirements and decrease calculation time. The model is made following the sample design diagram (Fig. 4.3) with a radius of 7.5 mm. The thicknesses of the film and the substrate layer are 1 μm and 5 mm respectively.

The 2D structured grids have an exponentially incremented meshing density from the model origin, where the heat source is located. Grid and time step independences tests are performed prior to the analysis: 70 divisions are used in both axial and depth directions, and the time step is determined to be 2×10^{-9} s.

Different from the analytical solution, the phase-lag values are not available explicitly in the numerical model. Instead, several cycles of the temperature response in the periodic quasi steady-state region are captured from the transient computation (Fig. 7.1) and the peak positions between the heat source and the temperature response with respect to time are compared to get the phase-lag profile (Fig. 7.2).

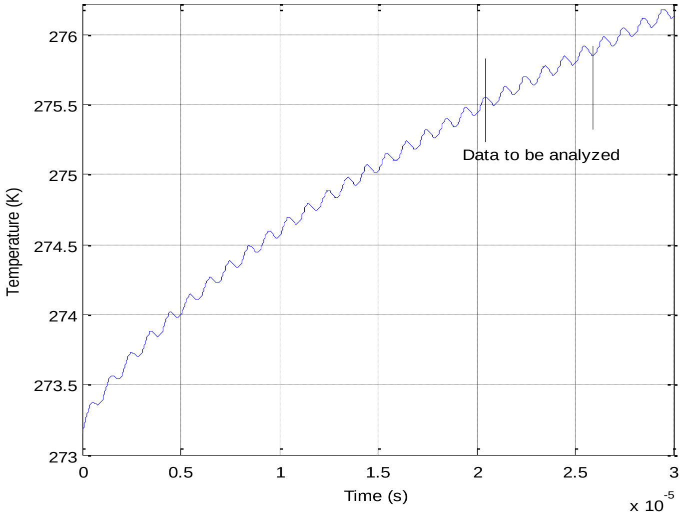

Figure 7.1 Obtaining the phase information of the temperature response from the numerical model.

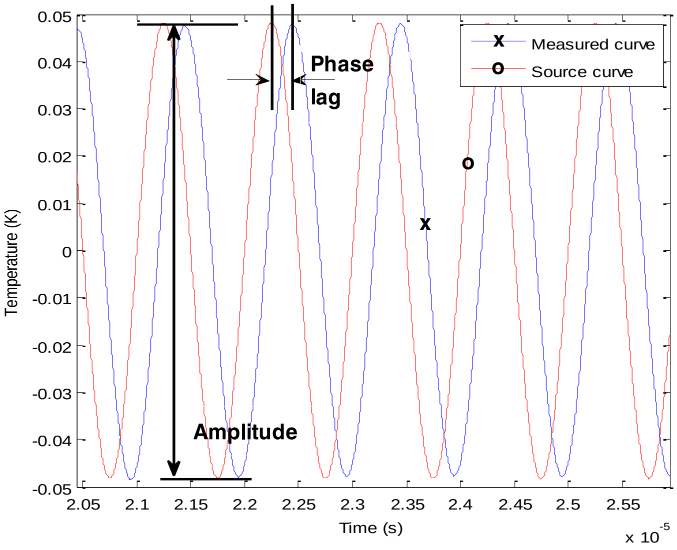

Figure 7.2 Phase-lag profile acquisition of the numerical model.

7.2. Simulation Results and Analysis

In order to validate the numerical model, the simulation results from the numerical model are plotted with the analytical solution in Fig. 7.3. Only surface heating was considered in the numerical model. With the interests of the probe laser distribution, one point temperature probe is located at the center of the heat source area (yellow triangle in Fig. 7.3), and another integral temperature probe is set at the center part of the heated area (brown triangle in Fig. 7.3). Heating laser spot radius and integral probe radius are assumed to be 15 and 5 μm respectively. The phase-lag deviations between the point probe and integral probe are found to be negligible. Both curves also overlap with the analytical solution (dark solid line in Fig. 7.3), validating the numerical model and leading to the conclusion that the influence of the probe laser size and distribution is trivial.

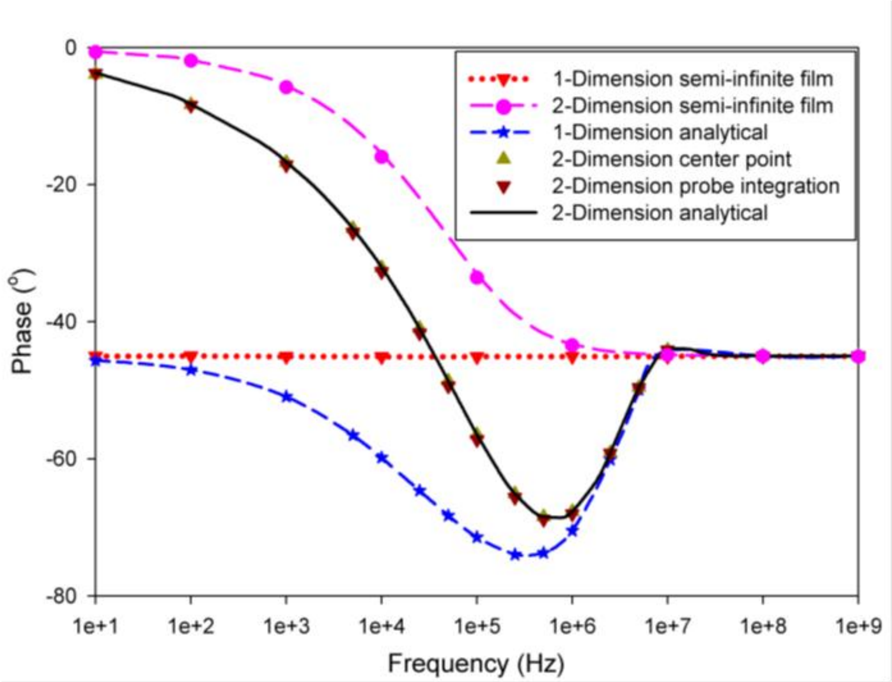

Figure 7.3 Simulation result from the numerical model to examine the influence of the size and intensity distribution of the probe laser to the experiment [56].

Calculation complexity from instant temperature changes prevents the temperature dependence of thermal conductivity from adding into the analytical solution, which is not a problem for the numerical model. It is especially important for CaF_2 sample, of which the temperature dependence of the thermal conductivity had been concluded as an important reason for the experimental error. Linear temperature dependence is assumed in our case because the temperature rise is expected to be less than 100 K. The temperature dependence coefficient is selected to be 0.05 K^{-1}, close to the real CaF_2 sample (0.04 K^{-1}). The results are plotted in Fig. 7.4. In the experimental frequency region (500 KHz – 2 MHz), a phase-lag deviation up to 10 degree is found (at 1 MHz the deviation is approximately 2 degree) between the analytical solution (dark solid line) and the simulation result with the consideration of temperature dependence of thermal conductivity (yellow triangle), which matches the experimental error analysis in Section 6.5.

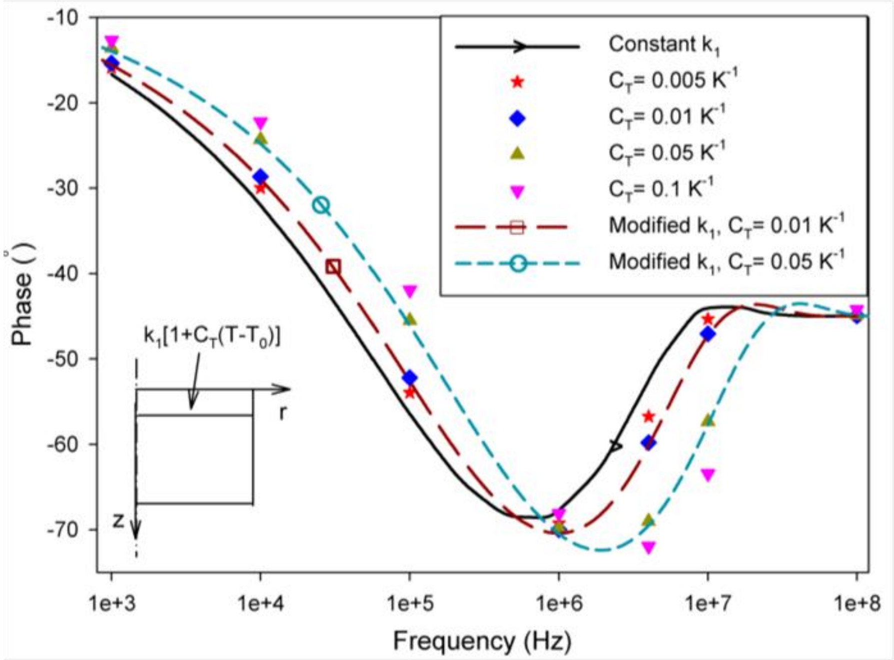

Figure 7.4 The influence of ks change caused by the temperature rise to the phase lag, simulated from the numerical model [56].

Although the temperature changes caused by surface convection and radiation are believed to be negligible compared to heat conduction, it is still of interest to quantify their influences with the powerful numerical model by adding them in the boundary conditions. A moderate convection heat transfer coefficient of 50 W·m^{-2}·K^{-1} and the emissivity of radiation of 0.1, 0.5 and 0.9 are used to simulate the natural environment. The results are plotted in Fig. 7.5. The deviation of the analytical solution and simulation is found less than 0.01% if the measurement frequency is above 10 KHz, which means the convection and radiation heat transfer can be safely ignored.

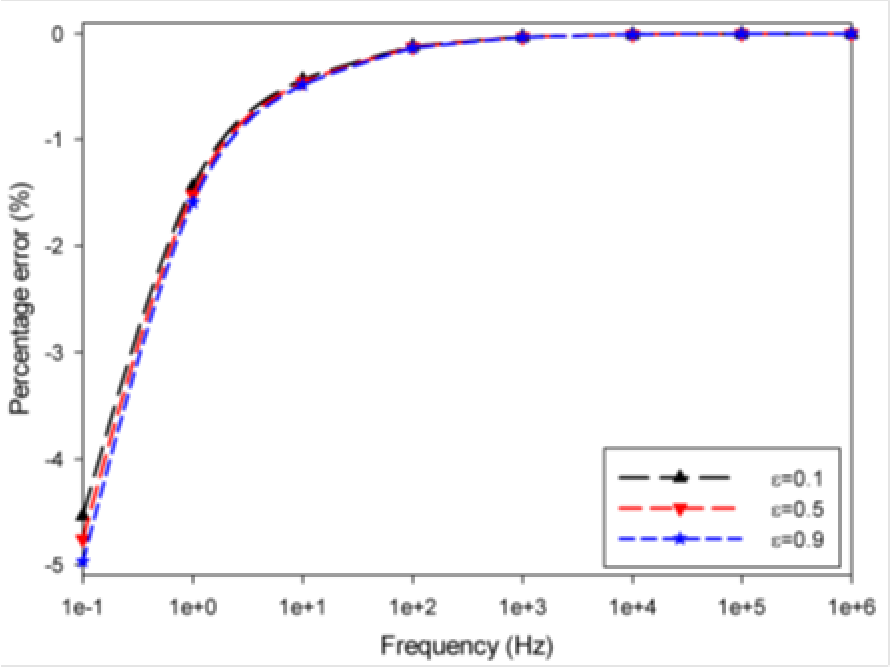

Figure 7.5 The experimental error caused by the convection and radiation heat transfer [56].

CHAPTER 8

ELASTICITY CONSTANTS DETERMINATION

Instead of measuring the thermal wave propagation, an extended application of the photothermal reflectance measurement setup is explored to measure the elasticity constants of solid materials from sensing the sample harmonic vibration. From a pump-probe approach with the use of fiber lasers, natural frequencies of cantilever beam samples are obtained. Similar to the thermal conductivity measurement, the intensity of the pump laser is modulated harmonically to heat the sample and excite different normal modes of vibration which are detected by the probe laser. Elasticity constants can be calculated from the measured natural frequencies.

Intrinsically, this technique is not sensitive to torsional modes of vibration. In this case, another technique, Laser-based Resonant Ultrasound Spectroscopy (LRUS), is prepared to capture them. In the LRUS technique, a rectangular, millimeter-sized sample is located on a specialized holder. By exciting the broadband resonant modes from a short-duration pulsed laser, the out-of-plane surface motion associated with the vibrational modes is detected by a photorefractive interferometer. An inverse fitting process based on Hamilton’s principle is then involved. After matching the measured vibrational modes with the simulated modes, the elasticity constants can be extracted.

In this chapter, the method to measure vibrational modes and obtain elasticity constants from a laser-involved reflectance approach is introduced. This method is validated by measuring the elasticity constants of rolled and annealed polycrystalline copper samples.

8.1. Introduction

Applying a stress on a solid material can cause deformation (strain). If the stress is below a critical value, the deformation is fully recoverable which means that the material will go back to its original shape without permanent deformation. This recoverable deformation is called elastic deformation and the critical stress is elastic limit (or yield strength). On the opposite, the stress above the elastic limit can cause permanent deformation which is named plastic deformation. It has been found that under elastic deformation, the strain (ε) is proportional to the applied stress (σ), or $\varepsilon=S\sigma$ (it's worth noting that not all elastic materials undergo linear elasticity deformation, e.g., many polymers). S is compliance constant. As an alternate, another form of this formula, $\sigma=C\varepsilon$, is also known as the Hooke's Law. C is elastic stiffness constant. In isotropic materials, it is the Young's modulus (E).

For most natural materials, the materials properties are orientation-dependent, which is defined as anisotropic. As opposed to anisotropic, if the properties of a material are the same in all orientations, the material is isotropic. A typical isotropic material is polycrystalline metal. For many polycrystalline materials, even though the individual grains are anisotropic, the property differences are "averaged" due to the random grain orientations and the overall bulk property can be isotropic.

Stress and strain are both orientation-dependent. Stress is defined as force per unit area, which not only depends on the magnitude and direction of the force but also on the orientation of the plane. Thus, specification of stress at a point requires a second-order tensor:

$$\sigma = \begin{bmatrix} \sigma_{xx} & \sigma_{xy} & \sigma_{xz} \\ \sigma_{yx} & \sigma_{yy} & \sigma_{yz} \\ \sigma_{zx} & \sigma_{zy} & \sigma_{zz} \end{bmatrix} \tag{8.1}$$

In the simple case of an axially loaded beam, only normal stress is generated, which is described by the orthogonal components of the stresses tensor. The other components are representative of the shear stresses. The most common case to generate shear stresses is bending from a shearing load. Similarly, strain is also a second-order tensor, composed of three normal strains and six shear strains components.

Correspondingly, both compliance (*S*) and stiffness (*C*) are fourth-order tensor with 81 (3^4) components. To describe elasticity of any material, all components are required to be clarified. Fortunately, the direct consequence of the symmetry in the stress and strain tensors (i.e., $\sigma_{ij}= \sigma_{ji}$) is that only 36 of the 81 components are independent and distinct terms. Moreover, this number can be decreased to 21 if the symmetry of the compliance (and stiffness) tensor is considered (i.e., $C_{ijkl}=C_{klij}$). Further deduction of the non-zero independent components in the compliance and stiffness tensor follows the fact that the crystal symmetry exerts influence on the symmetry of the physical property. It is also concluded as Neumann's principle: the symmetry elements of any physical property of a crystal must include all the symmetry elements of the point group of the crystal. The details of crystal symmetry of different materials and the relation of it to the independent elasticity constants are given in Section 8.2.

Before the discussion of the crystal symmetry, the matrix notations of the stress/strain and compliance/stiffness tensors are given first to simplify the tensor notation. The basic rules to convert the tensor indices to the matrix indices are: 11→1, 22→2, 33→3, 23→4, 13→5, and 12→6. For stress and stiffness tensor, this is the only rule to follow, e.g., σ_{22} (tensor notation) = σ_2 (matrix notation), C_{1232} (tensor notation) = C_{64} (matrix notation). For strain and compliance tensors, the situation is a little different due to the use of the engineering shear strain γ ($\varepsilon_{23} = \frac{1}{2} \gamma_{23} = \frac{1}{2} \varepsilon_4$, $\varepsilon_{13} = \frac{1}{2} \gamma_{13} = \frac{1}{2} \varepsilon_5$, and $\varepsilon_{12} = \frac{1}{2} \gamma_{12} = \frac{1}{2} \varepsilon_6$). For compliance tensor, $S_{ijkl} = S_{mn}$ when *m* and *n* are 1, 2, or 3, $2S_{ijkl} = S_{mn}$ when either *m* or *n* is 4, 5, or 6, and $4S_{ijkl} = S_{mn}$ when both *m* and *n* are 4, 5, or 6, e.g., $S_{1122} = S_{12}$, $2S_{1123} = S_{14}$, and $4S_{2323} = S_{44}$.

With the matrix notation, Hooke's Law can be rewritten as:

$$\begin{pmatrix} \sigma_1 \\ \sigma_2 \\ \sigma_3 \\ \sigma_4 \\ \sigma_5 \\ \sigma_6 \end{pmatrix} = \begin{pmatrix} C_{11} & C_{12} & C_{13} & C_{14} & C_{15} & C_{16} \\ C_{12} & C_{22} & C_{23} & C_{24} & C_{25} & C_{26} \\ C_{13} & C_{23} & C_{33} & C_{34} & C_{35} & C_{36} \\ C_{14} & C_{24} & C_{34} & C_{44} & C_{45} & C_{46} \\ C_{15} & C_{25} & C_{35} & C_{45} & C_{55} & C_{56} \\ C_{16} & C_{26} & C_{36} & C_{46} & C_{56} & C_{66} \end{pmatrix} \begin{pmatrix} \varepsilon_1 \\ \varepsilon_2 \\ \varepsilon_3 \\ \varepsilon_4 \\ \varepsilon_5 \\ \varepsilon_6 \end{pmatrix} \tag{8.2}$$

8.2. Symmetry Analysis and Independent Components

8.2.1. Symmetry of Crystal Materials

As mentioned previously, the number of independent components in the elasticity matrix depends on the symmetry of the crystal structures of the material. Different crystal structures have different rotational symmetric axes and different symmetries. For isotropic materials, because any axis can be considered as symmetry axis, there are only two independent elasticity constants: one to describe the flexural vibrational mode (*E*, or Young's modulus) and the other one to describe the torsional vibrational mode (*G*, or shear modulus). Vibrational modes are discussed in details in Section 8.3.

For anisotropic materials, the situation is more complicated. There are seven different anisotropic crystal structures, leading to various symmetries of the physical properties. The anisotropic crystal structures, corresponding symmetry system and the number of independent components in the compliance matrix are summarized in Table 8-1.

In this project, two most asymmetric cases (triclinic and monoclinic) are not considered. The detailed information of the common symmetries and their independent components are listed in Table 8-2.

8.2.2. Symmetry of Composite Materials

Unlike crystalline materials, the symmetry of fiber-based composite materials strongly depends on the ply orientation and stacking order. In this section, symmetries of four common used composite materials are checked: unidirectional, (0/90)s, (60/0/-60)s, and (0/45/-45/90)s.

An example of a unidirectional composite material is shown in Fig. 8.1. On the cross-section plane which is normal to the fiber orientation, the physical properties are symmetric with any axis/plane parallel to the fiber orientation. This special symmetry is defined as transverse isotropic. It can be easily proved that transverse isotropic materials exhibits hexagonal symmetry.

So the number of independent constants in the elasticity matrix is 5.

Table 8-1 Summary of the anisotropic crystal structure, corresponding symmetry system, the number of independent elasticity components, and examples.

Crystal structure	Rotational symmetric axes	# of independent components	example
Triclinic	none	21	Some minerals
Monoclinic	1 twofold (or 1 mirror plane)	13	Elemental sulfur
Orthorhombic	3 twofold	9	Wood
Tetragonal	1 fourfold	6	Some minerals
Trigonal	1 threefold	5	Quartz
Hexagonal	1 sixfold	5	Some minerals
Cubic	3 fourfold	3	Single crystal metals

Table 8-2 Detailed information of the independent elasticity constants in various anisotropic cases (isotropic case is added as a reference).

Crystal structure	# of independent components	Independent components
Orthorhombic	9	S_{11}, S_{22}, S_{33}, S_{12}, S_{13}, S_{23}, S_{44}, S_{55}, S_{66}. (The others components are 0)
Tetragonal	6	$S_{11}=S_{22}$, S_{33}, $S_{44}=S_{55}$, S_{66}, S_{12}, $S_{13}=S_{23}$
Hexagonal or Trigonal	5	$S_{11}=S_{22}$, S_{33}, S_{12}, $S_{13}=S_{23}$, $S_{44}=S_{55}$, $S_{66}=2(S_{11}-S_{12})$
Cubic	3	$S_{11}=S_{22}=S_{33}$, $S_{12}=S_{13}=S_{23}$, $S_{44}=S_{55}=S_{66}$
***Isotropic**	2	$S_{11}=S_{22}=S_{33}$, $S_{44}=S_{55}=S_{66}$, $S_{12}=S_{13}=S_{23}=S_{11}-\frac{1}{2}S_{44}$

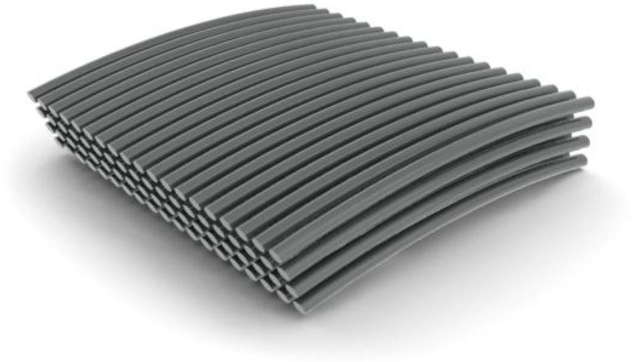

Figure 8.1 An example of unidirectional fiber.

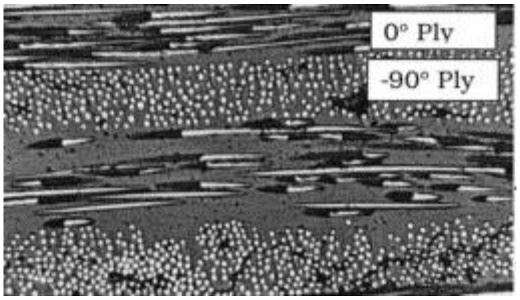

Figure 8.2 A cross-section picture of (0/90)s composites.

Fig. 8.2 shows a cross-section picture of (0/90)s composite materials. The plies with the orientations of 0 and 90 degree are stacked on each other alternately. The symmetry of (0/90)s composite materials is tetragonal because it has a fourfold rotational asymmetric axis, which means that rotating a (0/90)s composite material by 90 degree, the material properties will not be changed. A simple mathematical derivation can be performed from this rotational axis. The way to calculate the elasticity matrix components after rotation is:

$$S_{ijkl}' = a_{im}a_{jn}a_{ko}a_{lp}S_{mnop} \tag{8.3}$$

where S_{ijkl}' represents the elasticity constants after rotation, S_{mnop} represents the elasticity constants before rotation, and a is the rotational matrix with components depending on the angle of rotation. It is worth noting that tensor notations are used in both S and S' matrix instead of the matrix notation thus a conversion is required before using Eq. (8.3). Assume the orientation of the 0-degree ply is x_1, the orientation of the 90-degree ply is x_2, and the rotation happens with the axis of x_3, as plotted in Fig. 8.3, a matrix can be described as

$$a = \begin{bmatrix} 0 & 1 & 0 \\ -1 & 0 & 0 \\ 0 & 0 & 1 \end{bmatrix} \tag{8.4}$$

The elasticity constant S_{1111} after rotation will be [57]

$$S_{11}'=S_{1111}'=a_{11}a_{11}a_{11}a_{11}S_{1111}+a_{11}a_{11}a_{11}a_{12}S_{1112}+a_{11}a_{11}a_{11}a_{13}+S_{1113}+\ldots+a_{13}a_{13}a_{13}a_{13}S_{3333} \tag{8.5}$$

Assuming orthorhombic symmetry, there are only 9 non-zero independent components in the elasticity matrix (S_{11}, S_{12}, S_{13}, S_{22}, S_{23}, S_{33}, S_{44}, S_{55}, and S_{66}). Inserting these non-zero components (convert back to the tensor notation first) to Eq. (8.5), S_{11}' can be obtained as

$$S_{11}'=S_{1111}'=a_{12}a_{12}a_{12}a_{12}S_{2222}=S_{22}$$

It means that S_{11} of the rotated matrix and S_{22} of the original matrix are identical components. From the analysis above, S_{11} of the rotated matrix should equal to S_{11} of the original matrix. Therefore, S_{11} and S_{22} are equal (both in the original and rotated matrix)

Similarly,

$$\begin{aligned}
&S_{12}'=S_{1122}'=a_{12}a_{12}a_{21}a_{21}S_{2211}=S_{21}=S_{12}\\
&S_{13}'=S_{1133}'=a_{12}a_{12}a_{23}a_{23}S_{2233}=S_{23}\\
&S_{22}'=S_{2222}'=a_{21}a_{21}a_{21}a_{21}S_{1111}=S_{11}\\
&S_{23}'=S_{2233}'=a_{21}a_{21}a_{33}a_{33}S_{1133}=S_{13}\\
&S_{33}'=S_{3333}'=a_{33}a_{33}a_{33}a_{33}S_{3333}=S_{33}\\
&S_{44}'=4S_{2323}'=4a_{21}a_{33}a_{21}a_{33}S_{1313}=S_{55}\\
&S_{55}'=4S_{1313}'=4a_{12}a_{33}a_{12}a_{33}S_{2323}=S_{44}\\
&S_{66}'=4S_{1212}'=4a_{12}a_{21}a_{12}a_{21}S_{2121}=S_{66}
\end{aligned} \tag{8.5}$$

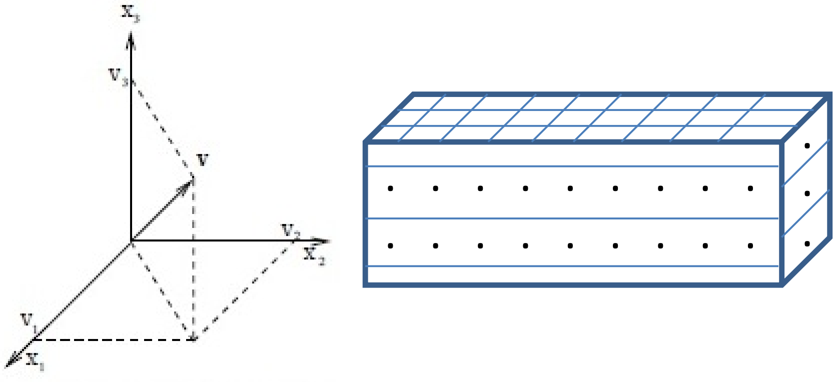

Figure 8.3 (0/90)s sample and the coordinates used in the derivation.

As a summary, $S_{11}=S_{22}$, $S_{13}=S_{23}$, $S_{44}=S_{55}$. Therefore the symmetry is tetragonal, with 6 independent elasticity constants.

Using the same way, the symmetry of (0/60/-60)s and (0/45/-45/90)s can both be proved as hexagonal (also called quasi-isotropic for composites), with 5 independent elasticity constants.

8.3. (0/90)s Sample and the Coordinates Used in the Derivation

8.3.1. Vibrational Mode and Natural Frequency

A normal mode of a vibration system is a pattern of motion in which all parts of the system move sinusoidally with same frequency with a fixed phase relation. The motion described by the normal modes is called resonance. The frequencies of the normal modes of a system are known as its natural frequencies. The normal modes of a physical object depend on its structure, materials and boundary conditions.

For a cantilever beam, there are two types of normal modes of vibration. One is the flexural mode including bending and lateral modes (Fig. 8.4(a) and (b)). The other one is the torsional mode (Fig. 8.4(c)). For isotropic materials, *E* and *G* are used to describe the flexural and

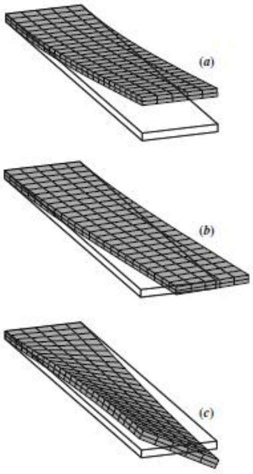

Figure 8.4 (a) Bending mode; (b) lateral mode; (c) torsional mode [58].

bending modes respectively. For anisotropic materials, the components in the top left area of the elasticity matrix (*i* and *j* equal to 1, 2 and 3) describe the flexural modes, and the components in the bottom right area (*i* and *j* equal to 4, 5 and 6) describe the torsional modes.

8.3.2. Relationship between Elasticity Constants and Natural Frequency

Two common methods can be used to measure natural frequencies. One is to supply a harmonic external excitation. If the frequency of the excitation source matches one of the natural frequencies of the system, resonance vibration can be activated and the vibrational energy will be stored by the system to increase the vibrational amplitude. By adjusting the frequency of the harmonic excitation and detecting the amplitude change of vibration, the natural frequencies can be found. This is the mechanism of the natural frequency measurements on the cantilever beam. The details are described in Section 8.3.3. The other method involves using short duration pulsed laser. One application is the LRUS technique which is introduced in Section 8.4.

Depending on the geometry of the cantilever beam, classical beam theories (e.g., Bernoulli-Euler beam theory, Timoshenko beam theory, etc.) are available to simplify and solve the governing equations without sacrificing accuracy. In this project, the beam is designed to be long and thin in order to match the requirements of the least complicated Bernoulli-Euler theory. From the classical solution of the Bernoulli-Euler beam theory, elasticity constants can be obtained from the sample density and geometry with a straight forward manner [58, 59].

The natural frequencies of the flexural modes are:

$$f_i^f = \frac{t}{4\pi}\left(\frac{\alpha_i^f}{L}\right)^2\sqrt{\frac{1}{3\rho S_{11}}} \tag{8.6}$$

where t and L are the thickness and length of the cantilever beam respectively, and ρ is the density. Superscription f represents the flexural mode and i is the order of the modes. α_i^f is obtained from $cosh\alpha_i^f cos\alpha_i^f + 1 = 0$, ultimately from the boundary conditions. For the torsional modes, the natural frequencies can be calculated from

$$f_i^t = \frac{2i-1}{4L}\sqrt{\frac{\zeta}{\rho I S_{44}}} \tag{8.7}$$

where I is the polar moment of the cross section and $I = \frac{1}{12}(tw^3 + wt^3)$ with w as the width of the beam. Superscription t represents torsional modes and ζ is calculated by

$$\zeta = \frac{1}{3}t^4\left(\frac{w}{t} - \frac{192}{\pi^5}\sum_{n=1}^{\infty}\frac{1}{n^5}tanh\frac{n\pi w}{2t}\right) \tag{8.8}$$

By measuring the natural frequencies of the flexural and torsional modes, two elasticity constants S_{11} and S_{44} can be obtained. By considering the orientation of the beam samples to the original material, more elasticity constants can be measured.

The experimental setup is designed for in-situ measurements. Due to the use of the fiber lasers, the whole setup is compact and easily embedded into harsh environments for real-time study. Located in a vacuum chamber inside a furnace, this system is able to measure the change of the elasticity constants with respect to temperature and pressure (e.g., heat treatments). Inside a nuclear reactor, this setup can perform the measurement on nuclear materials or materials under neutron irradiation (from which the microstructure change can be found).

8.3.3. Vibrational Modes Measurement from Photothermal Reflectance Setup

In this approach, the cantilever beam sample is manufactured from the original material with a frame surrounded as in Fig. 8.5. The sample is designed to be 17 mm long, 2 mm wide and 0.5 mm thick to reach the requirements of the Bernoulli-Euler theory (it's worth noting that the numerical model still shows a less than 2% error compare with the Timoshenko Beam Theory, suggesting an even longer beam length design). The surrounding frame is fixed to a specific module by screws at the corners. Extra pressure can be applied on the module to satisfy the cantilever beam boundary condition. The clamped end of the beam is shined by an intensity-modulated laser, and the thermal expansion difference at the top and bottom surface supplies an external excitation. The probe laser is focused on the free end of the beam and the reflected light is collected to sense the vibrations. When the frequency of the external excitation matches one natural frequency of the beam, resonant vibrations will be activated. The resulting amplitude of the free beam vibration will cause the intensity change of the reflected probe laser beam to reach a local maximum corresponding to the natural frequency.

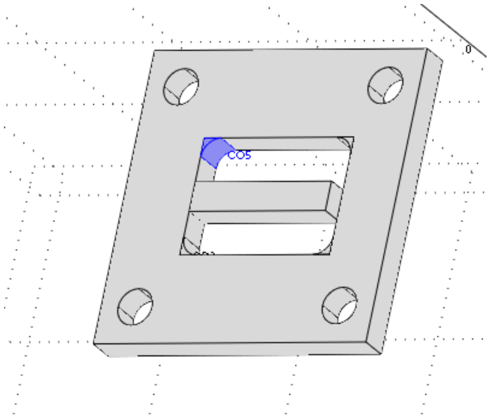

Figure 8.5 Design diagram of the cantilever beam sample.

This technique is particularly sensitive to the flexural modes (bending modes). From the vibration amplitude – modulation frequency curve, the natural frequencies of different vibrational modes can be obtained. However, because the clamped end is always the node (at which no vibration phenomena can be activated theoretically) of torsional modes, the torsional mode natural frequencies are intrinsically difficult to be captured from this technique. The laser-based resonant ultrasound spectroscopy will be required to capture the torsional model vibration.

8.4. Laser-based Resonant Ultrasound Spectroscopy (LRUS)

The other common method to measure the natural frequencies of a given sample is to use pulsed excitation to activate a superposition motion of several normal modes. This is the mechanism of the laser-based resonant ultrasound spectroscopy (LRUS) technique. In the LRUS technique, a high power pulsed laser is used to activate as many vibrational modes as possible. A probe laser or a photorefractive-interferometer scans the sample surface to get the out-of-plane motions at every position. The natural frequencies of the activated vibrational modes at each detection spot are then extracted by Fourier transform to obtain the resonant vibrational modes (spectroscopy). By recombining the amplitude information of all detection spots' vibration with respect to (natural) frequency, several resonant vibrational modes of the sample are acquired. An inverse fitting process based on Hamilton's principle is then performed. By matching the calculated vibrational modes with the measured modes at each frequency, the elasticity constants can be obtained. The unique advantage of the LRUS technique is that all independent elasticity constants can be theoretically fitted out from a single experiment run on one sample. However, the inverse fitting process in the LRUS technique has a sensitivity issue similar to the 3D frequency-domain photothermal reflectance technique (Section 4.1.3). Some published results from the LRUS technique shows that the elasticity constants of the isotropic sample (with 2 independent constants) can be measured with a great accuracy; however, on the samples having more than 3 independent elasticity constants (cubic or more asymmetric than cubic), only the ones relative to torsional modes can be accurately obtained. Therefore, it is recommended to identify the material symmetry before applying the LRUS technique on measuring elasticity constants of unknown samples.

8.5. Strategy to Measure Elasticity Constants

Theoretically, from the photothermal reflectance system, all elasticity constants can be measured if enough cantilever beam samples with necessary orientations are supplied. In real measurements, sensitivity becomes the first issue for reliable experimental results. As we stated previously, when the modulated excitation technique may not be sensitive enough for the torsional modes, LRUS can be used instead. The shear modulus, C_{44} (the mathematical reciprocal of S_{44}) had been successfully obtained on the polycrystalline copper sample by LRUS [60].

Another issue is the limitation of the beam orientations. For the original plate samples, the only possible axis of rotation is the one normal to the plate plane. It restricts the extraction of the elasticity constants which has to be measured from the four thin edges normal to the plate plane. The measureable elasticity constants from an original sample with plate shape are listed in Table 8-3.

The recipe of this measurement is given below:

1) manufacture cantilever beams following Fig. 8.5 from the original plate sample, with the orientations of 0 degree, 45 degree and 90 degree (the rotation axis is normal to the plate);
2) measure S_{11}, S_{22} from the flexural modes of the 0- and 90-degree samples separately (S_{11} and S_{22} are supposed to have the same value for materials with cubic, hexagonal, tetragonal or isotropic symmetry);
3) measure $2S_{12}+S_{44}$ from the flexural modes of the 45-degree sample;

Table 8-3 Measureable elasticity components of the independent ones*

Symmetry	# of independent elastic constants	# can be measured without torsional mode	# can be measured with torsional mode
Cubic	3 (S_{11}, S_{12}, S_{44})	2* (S_{11}, $2S_{12}$+S_{44})	3 (all)
Hexagonal	5 (S_{11}, S_{12}, S_{13}, S_{33}, S_{44})	1 (S_{11})	2 (S_{11}, S_{44}) 4 (S_{11}, S_{33}, S_{44}, S_{12}) for unidirectional
Tetragonal	6 (S_{11}, S_{12}, S_{13}, S_{33}, S_{44}, S_{66})	2* (S_{11}, $2S_{12}$+S_{66})	3 (S_{11}, $2S_{12}$+S_{66}, S_{44})
Orthotropic	9	3* (S_{11}, S_{22}, $2S_{12}$+S_{66})	5 (S_{11}, S_{22}, $2S_{12}$+S_{66}, S_{44}, S_{55})
*Isotropic	2 (S_{11}, S_{44})	1 (S_{11})	2 (both)

*note: although neither single value of S_{12} nor S_{44} can be measured from this step, one degree of freedom still diminishes from this relation, which also counts one “available elasticity constant” in Table 8-3

4) measure S_{44}, S_{55} from the torsional modes of the 0-degree sample and S_{66} from the 90-degree sample if the torsional modes are detectable; measure S_{44}, S_{55} and S_{66} from LRUS if the torsional modes are not sensed from the photothermal reflectance setup.

8.6. Experimental Results

Rolled and annealed polycrystalline Cu samples are selected as our validation samples. Measured by the electron backscatter diffraction (EBSD) technique, the structures of two polycrystalline Cu samples are both cubic with three independent components. The elasticity constants of the validation samples measured from other techniques (reported by Hurley et al. [61]) and this technique are listed in Table 8-4. The capability of the photothermal reflectance technique to sense torsional modes is proved on the rolled samples. On the annealed samples, no obvious torsional modes are captured and only the value of $2S_{12}+S_{44}$ is obtained from the flexural modes from the 45-degree sample. Due to the complexity of the LRUS technique and the corresponding inverse fitting process, we decide to make more attempts on measuring torsional modes from the annealed samples before LRUS is involved. The original experimental data (with the geometry information and natural frequencies in flexural modes) is given in Table 8-5.

An experimental error of ~10% is found in the measurement results, except for S_{12} of the rolled sample, which has an error of 21%. Briefly, the possible sources of experimental errors include the measurement errors of the size determination (length, thickness and width), inhomogeneity of the beam material, and the deviation of the measured length of the cantilever beams to the “effective length” (including the measured length and the contribution of the base that is also vibrating).

Table 8-4 Elasticity constants of the validation samples.

	Reported S_{11}	Reported S_{12}	Reported S_{44}	Measured S_{11}	Measured S_{12}	Measured S_{44}
Rolled sample	7.1×10^{-12}	-2.3×10^{-12}	23.3×10^{-12}	8×10^{-12} (13%)	-1.8×10^{-12} (21%)	25.6×10^{-12} (10%)
Annealed sample	12.7×10^{-12}	-5.1×10^{-12}	15×10^{-12}	13.8×10^{-12} (9%)	N/A	
		$2S_{12}+S_{44}=4.8\times10^{-12}$			$2S_{12}+S_{44}=4.2\times10^{-12}$ (12%)	

Table 8-5 Experimental data of the flexural modes and sample geometry, *E* represents effective elastic modulus.

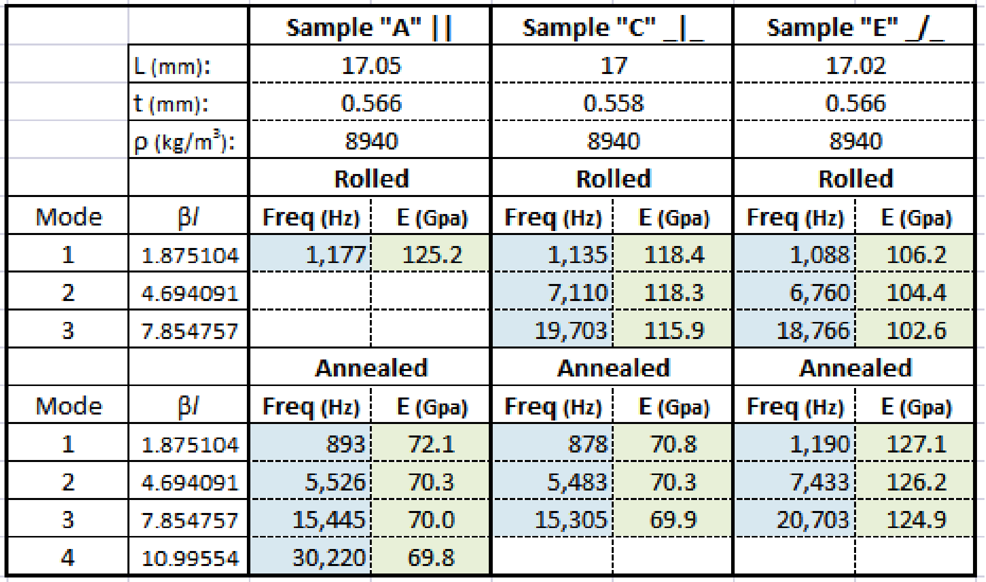

		Sample "A" ||		Sample "C" _|_		Sample "E" _/_	
	L (mm):	17.05		17		17.02	
	t (mm):	0.566		0.558		0.566	
	ρ (kg/m^3):	8940		8940		8940	
		Rolled		Rolled		Rolled	
Mode	β*l*	Freq (Hz)	E (Gpa)	Freq (Hz)	E (Gpa)	Freq (Hz)	E (Gpa)
1	1.875104	1,177	125.2	1,135	118.4	1,088	106.2
2	4.694091			7,110	118.3	6,760	104.4
3	7.854757			19,703	115.9	18,766	102.6
		Annealed		Annealed		Annealed	
Mode	β*l*	Freq (Hz)	E (Gpa)	Freq (Hz)	E (Gpa)	Freq (Hz)	E (Gpa)
1	1.875104	893	72.1	878	70.8	1,190	127.1
2	4.694091	5,526	70.3	5,483	70.3	7,433	126.2
3	7.854757	15,445	70.0	15,305	69.9	20,703	124.9
4	10.99554	30,220	69.8				

CHAPTER 9

CONCLUSIONS AND FUTURE WORK

A thermal conductivity measurement based on the photothermal reflectance technique was developed. Because of the use of lasers as heat source and probe, this measurement has some unique advantages including non-contact, non-destructive, fast, and high spatial-resolution (in the order of micrometer). In addition, the measurement can be performed on the sample with a size of millimeters, making this technique ideal to measure the thermal conductivity of nuclear fuels. Validation of this experimental setup was accomplished on two samples having thermal conductivity at both the upper and lower limit of the common range of nuclear fuels, and the results showed a great agreement to the literature values. As a post-irradiation examination tool, this new experimental approach has important technological applications to advance nuclear fuel development.

An extended application from the photothermal reflectance technique was explored to measure the elasticity constants on a cantilever-beam sample. The experimental results on polycrystalline copper samples agreed with the published values.

9.1. Conclusions

A thermal conductivity measurement system for solid materials was developed based on the photothermal methods with micrometer spatial-resolution. With specific treatments, this setup was optimized for measuring the samples with thermal conductivity in the range of 1 $W \cdot m^{-1} \cdot K^{-1}$ to 10 $W \cdot m^{-1} \cdot K^{-1}$ that is common for nuclear fuels. The experimental errors on validation samples, SiO_2 (1.4 $W \cdot m^{-1} \cdot K^{-1}$) and CaF_2 (9.2 $W \cdot m^{-1} \cdot K^{-1}$), were 3% and 16%, respectively. More experiments were applied on ZrO_2, glassy carbon, Zirconium and Chromium samples. Reliable experimental results were again obtained on the lower thermal conductivity samples (ZrO_2, 2

$W\cdot m^{-1}\cdot K^{-1}$, and glassy carbon, 6.3 $W\cdot m^{-1}\cdot K^{-1}$). The potentials of this setup on measuring thermal conductivity on good thermal conductors (Zr, 22.6 $W\cdot m^{-1}\cdot K^{-1}$, and Cr, 93.9 $W\cdot m^{-1}\cdot K^{-1}$) were also tested. System optimization will be needed if the sample is known to have a high thermal conductivity.

Due to the microstructure effect, thermal conductivity of the film needs to be measured before the substrate properties can be extracted from a reference sample. An approach of data refinement was designed to extract reliable film thermal conductivity from the raw data. The variation of the k_f values decreased from 60% before the refinement to 25%.

The experimental errors from the diffusivity measurement were smaller than the effusivity measurement. The sources of experimental errors on both measurements were discussed qualitatively for the possible improvements on measurement accuracy. For the diffusivity measurement, random error was dominating and increasing sample size can effectively decrease this type of error. For the effusivity measurement, the 1D heating condition was the most important factor for high reliability of experimental result. Uncertainty quantification was performed on both measurements and the overall uncertainty of the thermal conductivity determination (with CaF_2 sample as an example) was calculated to be 9.6%.

A numerical model was built and analyzed using the finite element simulation software COMSOL. The influences of some factors existing in real experiment but impossible to be considered in the analytical model were examined using the numerical model. The study on probe laser intensity distribution and heat convection and radiation validated the assumptions of the analytical model. The simulation result of temperature-dependent coefficient of thermal conductivity proved the conclusion in experimental error analysis that the temperature dependence of thermal conductivity of CaF_2 sample strongly influenced the measurement results.

The elasticity constants measurement was an extended exploration from the laser-based technique. Using pump laser to create a thermal expansion difference on top and bottom of the cantilever beam, the vibrational modes were activated and sensed by the probe laser. From measuring the natural frequencies of different vibrational modes, the elasticity constants were obtained. With different material symmetries, the available elasticity constants from this method were different. The material symmetries of crystal materials and composite materials were analyzed, and two polycrystalline materials with cubic material symmetry were selected as the validation samples. Torsional modes were observed on the rolled sample, but not on the annealed sample. The LRUS technique can be used as a complementary technique to measure the torsional modes. Experimental results on all measured properties compared favorably to the published values with about 10% errors.

9.2. Future Work

1) For the thermal conductivity measurement, a motorized stage to move the sample can be added in the setup to map the thermal-conductivity distribution. In order to provide the measurement-setup mobility, fiber lasers can be used instead of the diode lasers in current setup. It can also greatly simplify the light path alignment thus comfort the system maintenance.
2) For the elasticity constants measurement, although all three constants were measured on the rolled sample with acceptable experimental error, on the annealed sample the torsional mode was not captured. LRUS measurement will be performed if the situation is not improved. After that, elasticity constants measurements on more asymmetric materials will be attempted, and uncertainty quantification will be performed.

REFERENCES

[1] Incropera, F., Dewitt, D., Bergman, T., and Lavine, A., 2006, *Fundamentals of Heat and Mass Transfer*, John Wiley & Sons Inc, Hoboken, NJ.

[2] Berman, R., 1976, *Thermal Conductivity in Solids*, Clarendon, Oxford.

[3] Carslaw, H., and Jaeger, J., 1959, *Conduction of Heat in Solids*, Oxford University Press, London.

[4] 2013, "Wikipedia - Nuclear Power," from http://en.wikipedia.org/wiki/Nuclear_power.

[5] Cohen, I., Lustman, B., and Eichenberg, J. D., 1961, "Measurement of the Thermal Conductivity of Metal Clad Uranium Oxide Rods during Irradiation," J. Nucl. Mater., 3(3), pp. 331-353.

[6] Takahashi, Y., and Murabayashi, M., 1975, "Measurement of Thermal Properties of Nuclear Materials by Laser Flash Method," J. Nucl. Sci. Technol., 12(3), pp. 133-144.

[7] Sasahara, A., and Matsumura, T., 2008, "Post-irradiation Examinations Focused on Fuel Integrity of Spent BWR-MOX and PWR-UO_2 Fuels Stored for 20 Years," Nucl. Eng. Des., 238(5), pp. 1250-1259.

[8] Ångstrom, A., 1862, "Neue Methode, das Wärmeleitungsvermögen der Körper zu bestimmen," Ann. Phys., 190(12), pp. 513-530.

[9] Rosencwaig, A., and Gersho, A., 1976, "Theory of the Photoacoustic Effect with Solids," J. Appl. Phys., 47(1), pp. 64-69.

[10] Charpentier, P., Lepoutre, F., and Bertrand, L., 1982, "Photoacoustic Measurements of Thermal Diffusivity Description of the "Drum Effect"," J. Appl. Phys., 53(1), pp. 608-614.

[11] Mansanares, A., Bento, A., Vargas, H., Leite, N., and Miranda, L., 1990, "Photoacoustic Measurement of the Thermal Properties of Two-layer Systems," Phys. Rev. B, 42, pp. 4477-4486.

[12] Parker, W., Jenkins, R., Butler, C., and Abbott, G., 1961, "Flash Method of Determining Thermal Diffusivity, Heat Capacity, and Thermal Conductivity," J. Appl. Phys., 32(9), pp. 1679-1684.

[13] Nunes dos Santos, W., Mummery, P., and Wallwork, A., 2005, "Thermal Diffusivity of Polymers by the Laser Flash Technique," Polym. Test., 24(5), pp. 628-634.

[14] Min, S., Blumm, J., and Lindemann, A., 2007, "A New Laser Flash System for Measurement of the Thermophysical Properties," Thermochim. Acta, 455(1), pp. 46-49.

[15] Casalegno, V., Vavassori, P., Valle, M., Ferraris, M., Salvo, M., and Pintsuk, G., 2010, "Measurement of Thermal Properties of a Ceramic/Metal Joint by Laser Flash Method," J. Nucl. Mater., 407(2), pp. 83-87.

[16] Stonovic, 2012, "Wikipedia - Laser Flash Analysis," from http://en.wikipedia.org/wiki/Laser_flash_analysis.

[17] Olmstead, M., Amer, N., Kohn, S., Fournier, D., and Boccara, A., 1983, "Photothermal Displacement Spectroscopy: an Optical Probe for Solids and Surfaces," Appl. Phys. A Mater. Sci. Process., 32(3), pp. 141-154.

[18] Benedetto, G., Spagnolo, R., and Boarino, L., 1993, "Photothermal Displacement Technique: A Method to Determine the Variation of Thermal Conductivity versus Temperature in Silicon," Rev. Sci. Instrum., 64(8), pp. 2229-2232.

[19] Welsch, E., and Reichling, M., 1993, "Micrometer Resolved Photothermal Displacement Inspection of Optical Coatings," J. Mod. Opt., 40(8), pp. 1455-1475.

[20] Black, E. D., Grudinin, I. S., Rao, S. R., and Libbrecht, K. G., 2004, "Enhanced Photothermal Displacement Spectroscopy for Thin-film Characterization Using a Fabry-Perot Resonator," J. Appl. Phys., 95(12), pp. 7655-7659.

[21] Lepoutre, F., Balageas, D., Forge, P., Hirschi, S., Joulaud, J., Rochais, D., and Chen, F., 1995, "Micron-scale Thermal Characterizations of Interfaces Parallel or Perpendicular to the Surface," J. Appl. Phys., 78(4), pp. 2208-2223.

[22] Boccara, A., Fournier, D., and Badoz, J., 1980, "Thermo-optical Spectroscopy: Detection by the "Mirage Effect"," Appl. Phys. Lett., 36(2), pp. 130-132.

[23] Jackson, W. B., Amer, N. M., Boccara, A., and Fournier, D., 1981, "Photothermal Deflection Spectroscopy and Detection," Appl. Opt., 20(8), pp. 1333-1344.

[24] Murphy, J., and Aamodt, L., 1980, "Photothermal Spectroscopy Using Optical Beam Probing: Mirage Effect," J. Appl. Phys., 51(9), pp. 4580-4588.

[25] Skumanich, A., Dersch, H., Fathallah, M., and Amer, N., 1987, "A Contactless Method for Investigating the Thermal Properties of Thin Films," Appl. Phys. A Mater. Sci. Process., 43(4), pp. 297-300.

[26] Bertolotti, M., Dorogan, V., Liakhou, G., Li Voti, R., Paoloni, S., and Sibilia, C., 1997, "New Photothermal Deflection Method for Thermal Diffusivity Measurement of Semiconductor Wafers," Rev. Sci. Instrum., 68(3), pp. 1521-1526.

[27] George, S. D., Radhakrishnan, P., Nampoori, V., and Vallabhan, C., 2003, "Photothermal Deflection Measurement on Heat Transport in GaAs Epitaxial Layers," Phys. Rev. B, 68(16), p. 165319.

[28] Nordal, P. E., and Kanstad, S. O., 1979, "Photothermal Radiometry," Phys. Scripta, 20(5-6), p. 659.

[29] Santos, R., and Miranda, L., 1981, "Theory of the Photothermal Radiometry with Solids," J. Appl. Phys., 52(6), pp. 4194-4198.

[30] Tom, R. D., OHara, E. P., and Benin, D., 1982, "A Generalized Model of Photothermal Radiometry," J. Appl. Phys., 53(8), pp. 5392-5400.

[31] Tam, A., and Sullivan, B., 1983, "Remote Sensing Applications of Pulsed Photothermal Radiometry," Appl. Phys. Lett., 43(4), pp. 333-335.

[32] Martan, J., Herve, O., and Lang, V., 2007, "Two-detector Measurement System of Pulse Photothermal Radiometry for the Investigation of the Thermal Properties of Thin Films," J. Appl. Phys., 102(6), p. 064903.

[33] Horne, K., Ban, H., Mandelis, A., and Matvienko, A., 2012, "Photothermal Radiometry Measurement of Thermophysical Property Change of an Ion-irradiated Sample," Mater. Sci. Eng., B, 177(2), pp. 164-167.

[34] Weakliem, H., and Redfield, D., 1979, "Temperature Dependence of the Optical Properties of Silicon," J. Appl. Phys., 50(3), pp. 1491-1493.

[35] Rosencwaig, A., Opsal, J., Smith, W. L., and Willenborg, D., 1985, "Detection of Thermal Waves Through Optical Reflectance," Appl. Phys. Lett., 46(11), pp. 1013-1015.

[36] Reichling, M., and Gronbeck, H., 1994, "Harmonic Heat Flow in Isotropic Layered Systems and Its Use for Thin Film Thermal Conductivity Measurements," J. Appl. Phys., 75(4), pp. 1914-1922.

[37] Maznev, A., Hartmann, J., and Reichling, M., 1995, "Thermal Wave Propagation in Thin Films on Substrates," J. Appl. Phys., 78(9), pp. 5266-5269.

[38] Yagi, T., Taketoshi, N., and Kato, H., 2004, "Distribution Analysis of Thermal Effusivity for Sub-micrometer YBCO Thin Films Using Thermal Microscope," Physica C: Superconductivity, 412, pp. 1337-1342.

[39] Paddock, C. A., and Eesley, G. L., 1986, "Transient Thermoreflectance from Thin Metal Films," J. Appl. Phys., 60(1), pp. 285-290.

[40] Salazar, A., Sanchez-Lavega, A., and Terron, J., 1998, "Effective Thermal Diffusivity of Layered Materials Measured by Modulated Photothermal Techniques," J. Appl. Phys., 84(6), pp. 3031-3041.

[41] Li, B., Roger, J., Pottier, L., and Fournier, D., 1999, "Complete Thermal Characterization of Film-on-substrate System by Modulated Thermoreflectance Microscopy and Multiparameter Fitting," J. Appl. Phys., 86(9), pp. 5314-5316.

[42] Mansanares, A., Velinov, T., Bozoki, Z., Fournier, D., and Boccara, A., 1994, "Photothermal Microscopy: Thermal Contrast at Grain Interface in Sintered Metallic Materials," J. Appl. Phys., 75(7), pp. 3344-3350.

[43] Fanton, J., Mitzi, D., Kapitulnik, A., Khuri-Yakub, B., Kino, G., Gazit, D., and Feigelson, R., 1989, "Photothermal Measurements of High Tc Superconductors," Appl. Phys. Lett., 55(6), p. 598.

[44] Hua, Z., Ban, H., Khafizov, M., Schley, R., Kennedy, R., and Hurley, D. H., 2012, "Spatially Localized Measurement of Thermal Conductivity Using a Hybrid Photothermal Technique," J. Appl. Phys., 111(10), p. 103505.

[45] Hatori, K., Taketoshi, N., Baba, T., and Ohta, H., 2005, "Thermoreflectance Technique to Measure Thermal Effusivity Distribution with High Spatial Resolution," Rev. Sci. Instrum., 76(11), p. 114901.

[46] Bailey, J., Weber, E. R., and Opsal, J., 1990, "The Mechanism of Modulated Optical Reflectance Imaging of Dislocations in Silicon," J. Cryst. Growth, 103(1), pp. 217-225.

[47] Hurley, D., Khafizov, M., and Shinde, S., 2011, "Measurement of the Kapitza Resistance across a Bicrystal Interface," J. Appl. Phys., 109, p. 083504.

[48] Yarai, A., and Nakanishi, T., 2007, "Laptop Photothermal Reflectance Measurement Instrument Assembled with Optical Fiber Components," Rev. Sci. Instrum., 78(5), p. 054903.

[49] Stoner, R., and Maris, H., 1993, "Kapitza Conductance and Heat Flow between Solids at Temperatures from 50 to 300 K," Phys. Rev. B, 48(22), p. 16373.

[50] Polyanskiy, M., 2012, "Refractive Index Database," from http://refractiveindex.info/?group=METALS&material=Titanium.

[51] Thuau, D., Koymen, I., and Cheung, R., 2011, "A Microstructure for Thermal Conductivity Measurement of Conductive Thin Films," Microelectron. Eng., 88(8), pp. 2408-2412.

[52] Langer, G., Hartmann, J., and Reichling, M., 1997, "Thermal Conductivity of Thin Metallic Films Measured by Photothermal Profile Analysis," Rev. Sci. Instrum., 68(3), pp. 1510-1513.

[53] Hurley, D. H., and Lewis, R., 2007, "Coherent Control of Optically Generated and Detected Picosecond Surface Acoustic Phonons," J. Korean Phys. Soc., 51(1), p. 368.

[54] Ju, Y., and Goodson, K., 1999, "Phonon Scattering in Silicon Films with Thickness of Order 100 nm," Appl. Phys. Lett., 74(20), pp. 3005-3007.

[55] Slack, G. A., 1961, "Thermal Conductivity of CaF_2, MnF_2, CoF_2, and ZnF_2 Crystals," Phys. Rev., 122(5), p. 1451.

[56] Xing, C., Jensen, C., Hua, Z., Ban, H., Hurley, D. H., Khafizov, M., and Kennedy, J. R., 2012, "Parametric Study of the Frequency-domain Thermoreflectance Technique," J. Appl. Phys., (In Press).

[57] Nye, J. F., 1985, *Physical Properties of Crystals: Their Representation by Tensors and Matrices*, Oxford University Press, Oxford, NY.

[58] McFarland, A. W., Poggi, M. A., Bottomley, L. A., and Colton, J. S., 2005, "Characterization of Microcantilevers Solely by Frequency Response Acquisition," J. Micromech. Microeng., 15(4), p. 785.

[59] Graff, K. F., 1975, *Wave Motion in Elastic Solids*, Ohio State University Press, Columbus, OH.

[60] Hurley, D. H., Reese, S. J., and Farzbod, F., 2012, "Application of Laser-based Resonant Ultrasound Spectroscopy to Study Texture in Copper," J. Appl. Phys., 111(5), p. 053527.

[61] Hurley, D., Reese, S., Park, S., Utegulov, Z., Kennedy, J., and Telschow, K., 2010, "In Situ Laser-based Resonant Ultrasound Measurements of Microstructure Mediated Mechanical Property Evolution," J. Appl. Phys., 107(6), p. 063510.

APPENDICES

APPENDIX A

Derivation Details of Temperature Response of the 1D Model (with Thermal Resistance and Optical Absorption Considered)

The governing equations are rewritten by assuming that T_f and T_s have a thermal wave solution:

$$\frac{\partial^2 T_f}{\partial x^2} - \frac{i\omega}{D_f} T_f = -\frac{Q_0}{k_f}\exp(-\alpha x) \qquad 0<x<h \qquad \text{(A.1)}$$

$$\frac{\partial^2 T_s}{\partial x^2} - \frac{i\omega}{D_s} T_s = 0 \qquad x>h \qquad \text{(A.2)}$$

The boundary conditions are

$$-k_f \frac{\partial T_f}{\partial x}|_{x=0} = 0 \qquad \text{(A.3)}$$

$$k_f \frac{\partial T_f}{\partial x}|_{x=h} = k_s \frac{\partial T_s}{\partial x}|_{x=h} \qquad \text{(A.4)}$$

$$-R_{th} k_s \frac{\partial T}{\partial x}|_{x=h} = T_f - T_s \qquad \text{(A.5)}$$

The particular solution for the temperature on the surface (T_f) can be found from Eq. (A.1) by assuming that T_f is independent of time, which is

$$T_p = -\frac{Q_0}{k_f}\frac{1}{\alpha^2 - \sigma^2}\exp(-\alpha x)$$

where $\sigma = \sqrt{\frac{i\omega}{D_f}}$.

Therefore, T_f and T_s can be written as a combination of homogeneous solution and particular solution (for T_s, it's only the homogeneous solution), as below:

$$T_f = A\exp(\sigma x) + B\exp(-\sigma x) + T_p \qquad \text{(A.6)}$$

$$T_s = D\exp(\lambda x) + C\exp(-\lambda x) \qquad \text{(A.7)}$$

where $\lambda = \sqrt{\frac{i\omega}{D_s}}$.

It's worth noting that the substrate was assumed to be a semi-infinite solid. For the solution in the substrate to remain bounded, the coefficient *D* must equal zero. Therefore, Eq. (A.7) becomes $T_s = C\exp(-\lambda x)$.

In order to solve the coefficients *A*, *B*, and *C*, the boundary conditions are applied into Eq. (A.6) and (A.7).

Apply the boundary condition (A.3) to Eq. (A.6):

$$A = B - \frac{Q_0}{k_f}\frac{\alpha}{\sigma}\frac{1}{\alpha^2-\sigma^2} \tag{A.8}$$

Apply the boundary condition (A.4) to Eq. (A.6) and (A.7), and use Eq. (A.8) to cancel out the coefficient *A*:

$$C = -\frac{k_f}{k_s}\frac{1}{\lambda\exp(-\lambda h)}\{B\sigma[\exp(\sigma h) - \exp(-\sigma h)] + \frac{Q_0}{k_f}\frac{\alpha}{\alpha^2-\sigma^2}[\exp(-\alpha h) - \exp(\alpha h)]\} \tag{A.9}$$

The last step is to apply the boundary condition (A.5) to Eq. (A.6) and (A.7), and use Eq. (A.8) to cancel out the coefficient *A*:

$$-B[\exp(\sigma h) + \exp(-\sigma h)] + \frac{Q_0}{k_f}\frac{1}{\alpha^2-\sigma^2}\left[\frac{\alpha}{\sigma}\exp(\sigma h) + \exp(-\alpha h)\right]$$
$$= C(-R_{th}k_s\lambda - 1)\exp(-\sigma h)$$
$$\tag{A.10}$$

From Eq. (A.9) and (A.10), coefficients *B* and *C* can be calculated. It's worth noting that temperature response at the surface $T_{suf} = T_f\big|_{x=0} = A + B + T_p$, and the coefficient *A* can be calculated from Eq. (A.8) if the coefficient *B* is known. Therefore, T_{suf} can be obtained by calculating the coefficient *B* solely.

$$B = \frac{\frac{Q_0}{k_f}\frac{1}{\alpha^2-\sigma^2}\{\left[\frac{\alpha}{\sigma}\exp(\sigma h) + \exp(-\alpha h)\right] - \frac{\alpha}{\lambda}(R_{th}k_s\lambda + 1)\frac{k_f}{k_s}[\exp(-\alpha h) - \exp(\sigma h)]\}}{[\exp(\sigma h) + \exp(-\sigma h)] + \frac{\sigma}{\lambda}(R_{th}k_s\lambda + 1)\frac{k_f}{k_s}[\exp(\sigma h) - \exp(-\sigma h)]}$$

If T_s is needed, the coefficient C can be calculated from Eq. (A.9) or (A.10) by applying the expression of the coefficient B.

APPENDIX B

Derivation Details of Temperature Response of the 3D Model (with Anisotropic Thermal Conductivity, Thermal Resistance and Optical Absorption Considered)

The governing equations for heat conduction in both layers are given below:

$$k_{fij}T_{f,ij}-\rho_f c_f\dot{T}_f=Q_f \tag{B.1}$$

$$k_{sij}T_{s,ij}-\rho_s c_s\dot{T}_s=Q_s \tag{B.2}$$

and the heat source terms are

$$Q_f=\frac{P\alpha_f(1-R_f)}{\pi a_1 a_2}\exp(-\frac{x_1^2}{a_1^2}-\frac{x_2^2}{a_2^2}-\alpha_f x_3)(\frac{1}{2}+\frac{1}{4}(\exp(i\omega t)+\exp(-i\omega t))) \tag{B.3}$$

$$Q_s=\frac{P\alpha_s(1-R_f)(1-R_s)\exp(-\alpha_f h)}{\pi a_1 a_2}\exp(-\frac{x_1^2}{a_1^2}-\frac{x_2^2}{a_2^2}-\alpha_s(x_3-h))(\frac{1}{2}+\frac{1}{4}(\exp(i\omega t)+\exp(-i\omega t))) \tag{B.4}$$

The boundary conditions are essentially the same from the 1D model in Appendix A:

$$-k_{f3i}\frac{\partial T_f}{\partial z}|_{z=0}=0 \tag{B.5}$$

$$k_{f3i}\frac{\partial T_f}{\partial z}|_{z=h}=k_{s3i}\frac{\partial T_s}{\partial z}|_{z=h} \tag{B.6}$$

$$-R_{th}k_{s3i}\frac{\partial T}{\partial z}|_{z=h}=T_f-T_s \tag{B.7}$$

The normalization factors in Eq. (B.3) and (B.4) come from the following relationship

$$\int Q_f\,dv=P(1-R_f)$$

$$\int Q_s\,dv=P(1-R_f)(1-R_x)\exp(-\alpha_f h)$$

which implies

$$Q_{f0} = \frac{P\alpha_f(1-R_f)}{\pi a_1 a_2}$$

$$Q_{s0} = \frac{P\alpha_s(1-R_f)(1-R_s)\exp(-\alpha_f h)}{\pi a_1 a_2}$$

The solution procedure begins by assuming a thermal wave solution:

$$\check{T}_j = \frac{1}{2}(T_j \exp(i\omega t) + T_j^* \exp(-i\omega t)), \text{ for } j = s,f$$

Note the temperature is defined as real. Next, substitute the thermal wave solution into the diffusion equations and collect term in *exp(iωt)*:

$$k_{fij}T_{f,ij} - i\omega\rho_f c_f T_f = \frac{P\alpha_f\left(1-R_f\right)}{\pi a_1 a_2}\exp(-\frac{x_1^2}{a_1^2} - \frac{x_2^2}{a_2^2} - \alpha_f x_3)$$

$$k_{sij}T_{s,ij} - i\omega\rho_s c_s T_s = \frac{P\alpha_s(1-R_f)(1-R_s)\exp(-\alpha_f h)}{\pi a_1 a_2}\exp(-\frac{x_1^2}{a_1^2} - \frac{x_2^2}{a_2^2} - \alpha_s(x_3 - h))$$

Applying a 2D Fourier Transform to the heat conduction equations above with respect to x_1 and x_2 gives

$$-2\xi_1\xi_2 k_{f12}\hat{T}_f - 2i\xi_1 k_{f13}\hat{T}_{f,3} - 2i\xi_2 k_{f23}\hat{T}_{f,3} - \xi_1^2 k_{f11}\hat{T}_f - \xi_2^2 k_{f22}\hat{T}_f + k_{f33}\hat{T}_{f,33} - i\omega\rho_f c_f\hat{T}_f$$
$$= \frac{P\alpha_f\left(1-R_f\right)}{2\pi}\exp(-\frac{\xi_1^2 a_1^2}{4} - \frac{\xi_2^2 a_2^2}{4} - \alpha_f x_3)$$

$$-2\xi_1\xi_2 k_{s12}\hat{T}_s - 2i\xi_1 k_{s13}\hat{T}_{s,3} - 2i\xi_2 k_{s23}\hat{T}_{s,3} - \xi_1^2 k_{f11}\hat{T}_s - \xi_2^2 k_{f22}\hat{T}_s + k_{s33}\hat{T}_{s,33} - i\omega\rho_s c_s\hat{T}_s$$
$$= \frac{P\alpha_s\left(1-R_f\right)(1-R_s)\exp\left(-\alpha_f h\right)}{2\pi}\exp(-\frac{\xi_1^2 a_1^2}{4} - \frac{\xi_2^2 a_2^2}{4} - \alpha_s(x_3 - h))$$

The solution in transform space can be represented by

$$\hat{T}_f = A\exp\left(-\eta_f x_3\right) + B\exp\left(\eta_f x_3\right) + E\exp\left(-\alpha_f x_3\right) \qquad \text{for } x_3 \leq h$$

$$\hat{T}_s = C\exp(-\eta_s(x_3 - h)) + D\exp(\eta_s(x_3 - h)) + F\exp(-\alpha_s(x_3 - h)) \qquad \text{for } x_3 > h$$

The portion of the solutions with coefficients *E* and *F* correspond to the particular solution for the film and substrate respectively. For the solution in the substrate to remain bounded, the coefficient *D* must equal zero. The coefficient *A*, *B*, *C*, *E*, and *F* as well as the exponents $\eta_{f/s}$ are unknowns. The exponents $\eta_{f/s}$ are found by requiring that the homogeneous solutions satisfy the heat conduction equations:

$$k_{f33}\eta_f^2 + \left(2i\xi_1 k_{f13} + 2i\xi_2 k_{f23}\right)\eta_f - 2\xi_1\xi_2 k_{f12} - \xi_1^2 k_{f11} - \xi_2^2 k_{f22} - i\omega\rho_f c_f = 0$$

$$k_{s33}\eta_s^2 + (2i\xi_1 k_{s13} + 2i\xi_2 k_{s23})\eta_s - 2\xi_1\xi_2 k_{s12} - \xi_1^2 k_{s11} - \xi_2^2 k_{s22} - i\omega\rho_s c_s = 0$$

The coefficients E and F are found by substituting the particular solutions of the film and substrate into the respective differential equation:

$$E = \frac{\frac{P\alpha_f(1-R_f)}{2\pi}\exp(-\xi_1^2 a_1^2/4 - \xi_2^2 a_2^2/4)}{k_{f33}\alpha_f^2 + 2\alpha_f\left(ik_{f31}\xi_1 + ik_{f23}\xi_2\right) - 2\xi_1\xi_2 k_{f12} - k_{f11}\xi_1^2 - k_{f22}\xi_2^2 - i\omega\rho_f c_f}$$

$$F = \frac{\frac{P\alpha_s(1-R_f)(1-R_s)\exp(-\alpha_f h)}{2\pi}\exp(-\xi_1^2 a_1^2/4 - \xi_2^2 a_2^2/4)}{k_{s33}\alpha_s^2 + 2\alpha_s(ik_{s31}\xi_1 + ik_{s23}\xi_2) - 2\xi_1\xi_2 k_{s12} - k_{s11}\xi_1^2 - k_{s22}\xi_2^2 - i\omega\rho_s c_s}$$

The remaining coefficients, *A*, *B*, and *C* are found by satisfying the boundary conditions Eq. (B.5) – (B.7). The transformed boundary conditions are given by

$$(-ik_{f31}\xi_1\hat{T}_f - ik_{f32}\xi_2\hat{T}_f + k_{f33}\hat{T}_{f,3})\big|_{x_3=0} = 0$$

$$(-ik_{f31}\xi_1\hat{T}_f - ik_{f32}\xi_2\hat{T}_f + k_{f33}\hat{T}_{f,3})\big|_{x_3=h} = (-ik_{s31}\xi_1\hat{T}_s - ik_{s32}\xi_2\hat{T}_s + k_{s33}\hat{T}_{s,3})\big|_{x_3=h}$$

$$-R_{th}(-ik_{f31}\xi_1\hat{T}_f - ik_{f32}\xi_2\hat{T}_f + k_{f33}\hat{T}_{f,3})\big|_{x_3=h} = (T_f - T_s)\big|_{x_3=h}$$

Substituting the transformed solutions into the transformed boundary conditions gives the following system of equations

$$N \cdot \begin{bmatrix} A \\ B \\ C \end{bmatrix} = R$$

and

$$N_{11} = (-ik_{f31}\xi_1 - ik_{f32}\xi_2 - \eta_f k_{f33})$$

$$N_{12} = (-ik_{f31}\xi_1 - ik_{f32}\xi_2 + \eta_f k_{f33})$$

$$N_{13} = 0$$

$$N_{21} = (-ik_{f31}\xi_1 - ik_{f32}\xi_2 - \eta_f k_{f33})\exp(-\eta_f h)$$

$$N_{22} = (-ik_{f31}\xi_1 - ik_{f32}\xi_2 + \eta_f k_{f33})\exp(-\eta_f h)$$

$$N_{23} = (ik_{s31}\xi_1 + ik_{s32}\xi_2 + \eta_s k_{s33})$$

$$N_{31} = R_{th}\left(ik_{f31}\xi_1 + ik_{f32}\xi_2 + \eta_f k_{f33}\right)\exp\left(-\eta_f h\right) - \exp\left(-\eta_f h\right)$$

$$N_{32} = R_{th}\left(ik_{f31}\xi_1 + ik_{f32}\xi_2 - \eta_f k_{f33}\right)\exp\left(\eta_f h\right) - \exp\left(\eta_f h\right)$$

$$N_{33} = 1$$

$$R_1 = E(ik_{f31}\xi_1 + ik_{f32}\xi_2 + \alpha_f k_{f33})$$

$$R_2 = E(ik_{f31}\xi_1 + ik_{f32}\xi_2 + \alpha_f k_{f33})\ \exp\left(-\alpha_f h\right) - F(ik_{s31}\xi_1 + ik_{s32}\xi_2 + \alpha_s k_{s33})$$

$$R_3 = E[1 - R_{th}\left(ik_{f31}\xi_1 + ik_{f32}\xi_2 + \alpha_f k_{f33}\right)]\ \exp\left(-\alpha_f h\right) - F$$

VITA

Zilong Hua
Mechanical & Aerospace Engineering
Utah State University
Phone: (435)764-6725

Email: zilong.hua@aggiemail.usu.edu
4130 Old Main Hill
Logan, Utah 84322-4130

EDUCATION

Dec. 2012	Utah State University, Logan, UT Ph.D. in Mechanical Engineering Dissertation topic: *Hybrid Photothermal Technique for Microscale Thermal Conductivity Measurement* Major Advisor: Prof. Heng Ban
June 2007	Tsinghua University, Beijing, China B.S. in Materials Sciences and Engineering Thesis topic: *Firmware Programming for a lab-used furnace using LabVIEW*

RESEARCH EXPERIENCE

2011-2012 Idaho National Laboratory

Research Intern, Department of Material Science and Engineering

- Designed and developed a laser-based photothermal reflectance system to measure thermal conductivity of solid materials with micrometer spatial resolution

- Developed and improved a fiber-laser measurement system to obtain elasticity constants of solid materials; observed and analyzed influences of material annealing and recrystallization on its elastic performances
- Performed Laser-based Resonant Ultrasonic Spectroscopy (LRUS) technique to measure elasticity constants of solid materials
- Programmed firmware for the measurement systems using MATLAB
- Optimized the measurement systems by simulating experimental procedures and performing parametric analysis using MATLAB and COMSOL

2008-2008 Idaho National Laboratory

Summer Intern, Department of Material Science and Engineering

- Derived and improved a theoretical model for thermal effusivity measurement

2007-2012 Utah State University

Graduate Research Assistant, Department of Mechanical and Aerospace Engineering

- Designed and developed a laser-based photothermal reflectance system (from scratch) to measure thermal effusivity of solid materials with micrometer spatial resolution
- Directed and assisted for a fiber-laser photothermal reflectance system development

2006-2007 Tsinghua University, Electron Microscopy Laboratory

Undergraduate Research Assistant, Department of Materials Science and Engineering

- Programmed firmware for a lab-used furnace using LabVIEW

- Observed and studied the Giant Magnetoresistance (GMR) effect in Co-C granular films prepared on Si substrates

TEACHING EXPERIENCE

2013- Utah State University

Teaching Assistant

- Lectured recitation for an undergraduate course “Heat and Mass Transfer”

2007-2010 Utah State University

Teaching Assistant

- Graded homework and test papers for undergraduate courses “Solid Mechanics”, “Heat and Mass Transfer”, and a graduate course “Finite Element”

PUBLICATIONS

Peer-Reviewed Journal Publications

Z. Hua, H. Ban, M. Khafizov, R. Schley, R. Kennedy, and D. Hurley, “Spatially localized measurement of thermal conductivity using a hybrid photothermal technique”, Journal of Applied Physics, 111, pp. 103505(2012)

C. Xing, C. Jensen, Z. Hua, H. Ban, D. Hurley, M. Khafizov, and R. Kennedy, “Parametric study of the frequency-domain thermoreflectance technique”, Journal of Applied Physics, (submitted)

Peer-Reviewed Conference Presentations and Papers

Z. Hua, M. Khafizov, D. Hurley, H. Ban and R. Kennedy, “Laser-based measurement of thermal conductivity with micrometer spatial resolution”, *18th Symposium on thermophysical properties*, Boulder, CO, June 2012

H. Ban and Z. Hua, “Laser flash measurement of samples with a transparent reference layer”, *ASME 2009 Heat Transfer Summer Conference collected with the InterPACK09 and 3rd Energy Sustainability Conference (HT2009)*, San Francisco, CA, July 2009

C. Xing, Z. Hua and H. Ban, “Evaluation of uncertainties of one-directional analytical model for thermoreflectance technique”, *ASME 2011 8th Thermal Engineering Joint Conference*, Honolulu, HI, March 2011

R. Schley, D. Hurley and Z. Hua, “Optical fiber technique for in-reactor mechanical properties measurement”, *Conference: Review of Progress in Quantitative Nondestructive Evaluation*, Denver, CO, July, 2012

HONORS AND AWARDS

- 3rd place in 2009 Intermountain Graduate Research Symposium

PROFESSIONAL GROWTH AND DEVELOPMENT ACTIVITIES

- Served as the communication generic officer in American Nuclear Society Nuclear Club in Utah State University
- Served as conference assistant in Materials Research Society 2011 Fall Conference

COMPUTER SKILLS

- Programming Languages: C/C++ , FORTRAN
- Software Packages: MATLAB, LabVIEW, COMSOL, FEMAP